

**LANDSLIDE SUSCEPTIBILITY AND GROUND DISPLACEMENT
ASSESSMENT OF AUSTIN CITY AND ITS SURROUNDINGS**

by

ROSBEIDY HERNÁNDEZ

Bachelor in Geological Engineering
Universidad Central de Venezuela
Caracas, Venezuela

Submitted to the Graduate Faculty of
the College of Science and Engineering
Texas Christian University
in partial fulfillment of the requirements for the degree of

Master of Science

August 2022

**LANDSLIDE SUSCEPTIBILITY AND GROUND DISPLACEMENT
ASSESSMENT OF AUSTIN CITY AND ITS SURROUNDINGS**

By

Rosbeidy Hernández

Approved by:



Dr. Esayas Gebremichael (Major Professor)



Dr. Helge Alsleben



Mohamed Ahmed (Jul 20, 2022 14:36 CDT)

Dr. Mohamed Ahmed

For the College of Science and Engineering

Copyright by
Rosbeidy Hernández
2022

ACKNOWLEDGMENTS

First of all, I would like to thank God for being my guide, my hope, and my shelter.

Special thanks to Dr. Gebremichael for allowing me to learn from him and to do research in his area of expertise. I also thank my committee members, Dr. Alsleben and Dr. Ahmed, for allowing me to successfully carry this project to the end.

I would like to thank the faculty members, for always having an answer for all my questions for your guidance along these two years. Special to Dr. Xie for encouraging me to apply to TCU, as well as Dr. Harvey, and Dr. Denne for helping me throughout my master's program including my degree project.

To the Science & Engineering Research Center, for providing resources to develop my research.

To my classmates, for making this journey easier. Special thanks to Benite and Yosef from the Remote Sensing team.

To my professor from my home university UCV, Dr. Urbani, for introducing me to this fantastic world of geology. And for always being there present in my personal and academic achievements.

To my family, for always being there for me, and supporting my dreams and goals with their love. To my parents, my siblings, niece, and nephews, who despite not being physically here with me are still my strength and biggest support. To my cousins, Gabo, Lili, Cesar y Ana (who became my brightest start in the heaven when I was in my fieldtrip) you all have been my support and motivation. To my mother-in-law for having so much patience and being there helping us.

To my uncle Nelson, Circe, Estefania, and Daniela for being there always and by extending their hand whenever they can, including all the Gomez family for each encouraging word in this process. To Sandra and Jose V. for receiving us when I arrived here to Texas and giving me the best guidance and support for my development here.

I would not leave out my support team of laughs and tears: my family from Fort Worth, Dama and Robert, Caro, Matt, and Carol. You are part of this history. Also, my best friend Alejandra, who has been there for me; you have been my rib and my breath in many moments, and in this one you have been so important.

And last but not least, I would like to thank to husband Ali Gomez, who has always inspired me with his love and respect. Thank you for continuously pushing me to move forward, and for navigating this life together, through ups and downs, always growing through it all. You have been my main pillar and support in making this project possible. And of course, now that our family is growing, for sure I know you will be the best daddy.

TABLE OF CONTENTS

1.	INTRODUCTION	1
1.1.	Research roadmap	1
1.2.	Background	2
1.3.	Geospatial Datasets and Techniques for Investigating Landslide Hazards	6
1.3.1.	GIS for Landslide Studies	7
1.3.2.	Remote Sensing on Landslide Studies.....	9
2.	STUDY AREA, OBJECTIVES, AND SIGNIFICANCE	11
2.1.	The study area	11
2.2.	Statement of the problem.....	12
2.3.	Research Questions, Objectives, and Significance	13
3.	GEOLOGIC, HYDROLOGIC, AND CLIMATIC SETTINGS.....	15
3.1.	Geography, Climate, and Hydrology.....	15
3.2.	Geological Framework	16
3.2.1.	Regional Geology	16
3.2.2.	Local Geology	17
4.	DATA AND METHODS	22
4.1.	Overview	22
4.2.	Landslide Susceptibility Mapping (LSM)	23
4.2.1.	Controlling Factors	23
i.	Slope Gradient	24
ii.	Land Cover	24
iii.	Local Geology and Geological Structures	25
iv.	Drainage Network and Precipitation Data.....	27
4.2.2.	Landslide Susceptibility Index	28
4.3.	Detecting and Quantifying Slow-Moving Landslides	29
4.3.1.	SAR Datasets.....	29
4.3.2.	Surface Deformation Estimation using InSAR.....	33
4.3.3.	Small Baseline Subset (SBAS).....	36
4.3.3.1	Calibration and Validation - Global Navigation Satellite System (GNSS) Data	39
i.	Permanent stations.....	40
ii.	Campaign measurements	41
4.4.	Ancillary Data and Methods.....	43
4.4.1.	Soil Texture Analysis	44
4.4.2.	Unmanned Aircraft Systems (UAS).....	45

5. RESULTS AND DISCUSSION.....	46
5.1. Overview	46
5.2. Analyses of Factors Controlling Landslide Susceptibility	46
5.3. Landslide Susceptibility Map	58
5.4. SBAS	64
5. CONCLUSION	70
6. REFERENCES	72

VITA

ABSTRACT

LIST OF FIGURES

Figure 1 Representation of forces acting on a block on an inclined plane	3
Figure 2 Types of landslides based on behavior and speed in which material moves	4
Figure 3 Location map of the study area. The green dot shows the location reference of the slope failure in the Pease Park which is located along the trail of the Shoal Creek.....	12
Figure 4 Google Earth images of the Pease Park located along the Shoal Creek before (a) and after (b) the first slope failure event (2018).	13
Figure 5 Travis County (red box) reference location in physical regions of Texas (Butler, 2021).....	17
Figure 6 . S Spatial distribution of the geological units and faults in the study area retrieved from the Geologic Atlas of Texas: Austin Sheet (Barnes et al., 1981).....	19
Figure 7 Massive Block of the Buda Formation on top of the Del Rio Formation (part of the material from the slope failure incident on Pease Park).....	20
Figure 8 Diagram of Cretaceous lithologic units and zonal stages of formations in Texas. Note that the Buda Formation overlies the Del Rio Formation (taken from R. A. Denne, 2022, unpublished data)	21
Figure 9. SAR image acquisition geometry. The radar sensor flight along the azimuth direction at an altitude H observing the Earth's surface at an oblique look angle θ_t . The illuminated footprint size is based on the antenna Beam width β , and the distance from the sensor to the ground R (Flores-Anderson, et al. 2019).....	31
Figure 10. InSAR deformation geometry. In A (Pass/flight 1), a ground surface is imaged. In B (Pass 2), the satellite passes over the same area.....	34
Figure 11 SBAS Interferometric images connection graph, time, and position plot derived from the fifty-three Sentinel-1 images acquired over the study area. The yellow dot signifies the super reference image, selected by the software, that was used as a reference for the coregistration procedure.	38
Figure 12 SBAS data processing flowchart (Chen et al., 2021).....	39
Figure 13 TXAU station daily position data graph from (1996–present).	41

Figure 14 RTK GNSS measurements during the second campaign (March 2022).....43

Figure 15 Slope analysis map of the study area derived using high-resolution LiDAR DEM.....47

Figure 16 The spatial distribution of the different land cover types of the study area..49

Figure 17. Classification of the geological units in the study area based on the perceived cohesive strengths and stability of the units.52

Figure 18 Fault and fracture buffer zones indicating the susceptibility of areas to landslide based on their proximity to the structures. Areas located within 500-m radius of the features are considered highly susceptible to landslide hazards.....53

Figure 19 Inferred tectonic features of the study area based on Sentinel-1 SAR image and DEM data.54

Figure 20 Drainage buffer zones indicating the susceptibility of areas to landslide based on their proximity to drainage networks.....56

Figure 21 Classification of the study area based on the amount of mean precipitation received (1981 – 2019).....57

Figure 22 Landslide susceptibility map of Austin City and surroundings.60

Figure 23 A 3D model of the Pease Park (Shoal Creek) landslide created using data acquired by the UAS. The fractured and weathered Buda limestone is shown overlying the Del Rio clay. The fracture paths within the limestone layer through which water from the surface percolates into the subsurface and interact with the Del Rio clay layer are shown in red.63

Figure 24 Soil texture triangle depicting the textural composition of the samples collected from the Pease Park (Shoal Creek)..64

Figure 25 (a) Surface deformation analysis of the study area derived using the SBAS technique applied on SAR datasets. The three sites that were selected for field assessment to determine the causes of the high subsidence rates are shown in red-outlined boxes. The Pease Park area where recent landslides have occurred is shown in a black-outlined box; (b) Time-lapse (2015 – 2021) Google Earth images of the investigated sites (A, B, and C) were visited.....66

Figure 26 Areas surrounding the Pease Park landslide show signs of active displacement activity (tilted trees on the left, and bent stem on the right) that supports the slow rate of displacement estimated using the SBAS technique (Figure 25).....68

LIST OF TABLES

Table 1 Most commonly used microwave bands in past and current SAR sensors with correlated frequency, wavelength, and known applications.....	29
Table 2 Sentinel-1 scenes used in this study that were acquired along orbital track 107.....	33
Table 3 Lithological Classification of the study area	51
Table 4 Weight and rating assigned to each of the controlling factors	59
Table 5 Analysis indicating the area and percentage coverage of the landslide susceptibility categories..	60
Table 6 . Displacement rate (given in mm/month) calculated using multi-temporal (7-month interval) GNSS RTK measurements	69

CHAPTER ONE

INTRODUCTION

1.1. Research roadmap

The present research seeks to provide a better understanding of ground surface deformation processes associated with slow-moving landslides and the triggering factors in Austin City and its environs. Austin and its suburbs have witnessed a high rate of population growth and spatial expansion of the city in the last two decades increasing the residents' vulnerability to the impacts of a landslide hazard. This vulnerability was observed in the Shoal Creek area of Austin, where two consecutive landslides occurred around Pease Park, one in May 2018 and the second in May 2019. These two landslide events indicated the possible susceptibility of parts of the Austin and outlying areas to a landslide hazard. Hence, the city was selected in this study to demonstrate the vulnerability of communities living in landslide-susceptible settings. Several analytic techniques were implemented in this study to detect areas that are susceptible to future landslides events, with emphasis on slow-moving types whose progressive movement can be detected, so that appropriate mitigation efforts can be implemented to reduce their impacts on communities and resources.

This work is organized into six major chapters. Chapter 1 provides a background of landslide processes, types of landslides, and various datasets and approaches used in previous studies to map landslide susceptibility with a primary focus on GIS and remote sensing techniques.

Chapter 2 provides an overview of the study area, the objectives of the research; chapter 3 describes the climate and hydrology of the study area. In addition, detailed description of regional and local geological units is provided.

Chapter 4 describes comprehensive information on the datasets and methodologies applied for the landslide susceptibility and ground displacement assessment in the city of Austin and its

surroundings with data between 2015 and 2021. This chapter also discusses software and techniques used along with data collection campaigns for validation and calibration purposes.

Chapter 5 is dedicated to discussing the results for the landslide susceptibility and ground displacement assessment in the city of Austin and its surroundings. The findings and interpretations derived using the individual methods/techniques are described separately. In addition, the collective effects and relevance of each of the derived interpretations which contribute to the hazard, and to the various objectives of the study are discussed as well.

Finally, Chapter 6 summarizes the findings and interpretations of the present study. The chapter also includes recommendations regarding mitigating landslide hazard's potential effects and ways to assess further its impact in and around the city of Austin. It also has addition/inclusion of new datasets and observations in future studies.

1.2. Background

A landslide is one type of mass-wasting in which a mass of rock, debris, or earth moves down a slope driven by the force of gravity. Slope gradient is one of the crucial factors that control the occurrence of a landslide phenomenon and additionally, it is a key component of slope stability analysis (Dai et al., 2001; Firomsa and Abay, 2019). The slope gradient factor impacts a landslide event whenever the downward pull of gravity (f_g) exceeds the resisting forces (Wachal and Hudak, 2000). That is, a landslide could occur when the shear/driving force (f_s) exceeds normal force (f_n) owing to a steeper slope or if the earth material erodes and lowers the shear strength (Figure 1) (Johnson et al., 2017)

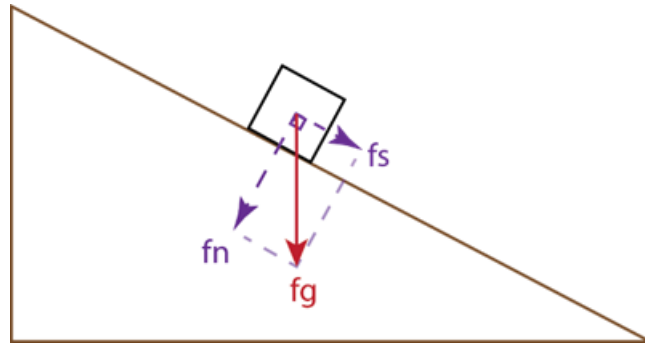


Figure 1: Representation of forces acting on a block on an inclined plane. The parameter f_g refers to the force of gravity while f_s and f_n represent the shear/driving force and normal force, respectively (Johnson et al., 2017)

Landslide phenomena are one of the major natural hazards that result in severe economic, human, and environmental losses (Chalkias et al., 2014). Various types of landslides exist with the classification being primarily dependent on the composition of the materials and the type of movement of the materials down a slope. These include slides (debris slide, rock compound slide), falls, slip, slump, topple, flows (Earth Flow, Debris Flow), creep, and avalanche (Varnes, 1958; Glade et al., 2006; Yilmaz et al., 2012; Hungr et al., 2014). Though most landslides fall in one of the above-stated landslide type categories, some landslides are expressed as combinations of several types of slides (Figure 2a). Rock falls, topples, and debris avalanches are commonly associated with failures in mountainous areas with harder rock compositions, whereas earth flows and creep landslides are commonly associated with steep topographical zones composed of soft sedimentary rock material (Varnes, 1978; Glade et al., 2006)

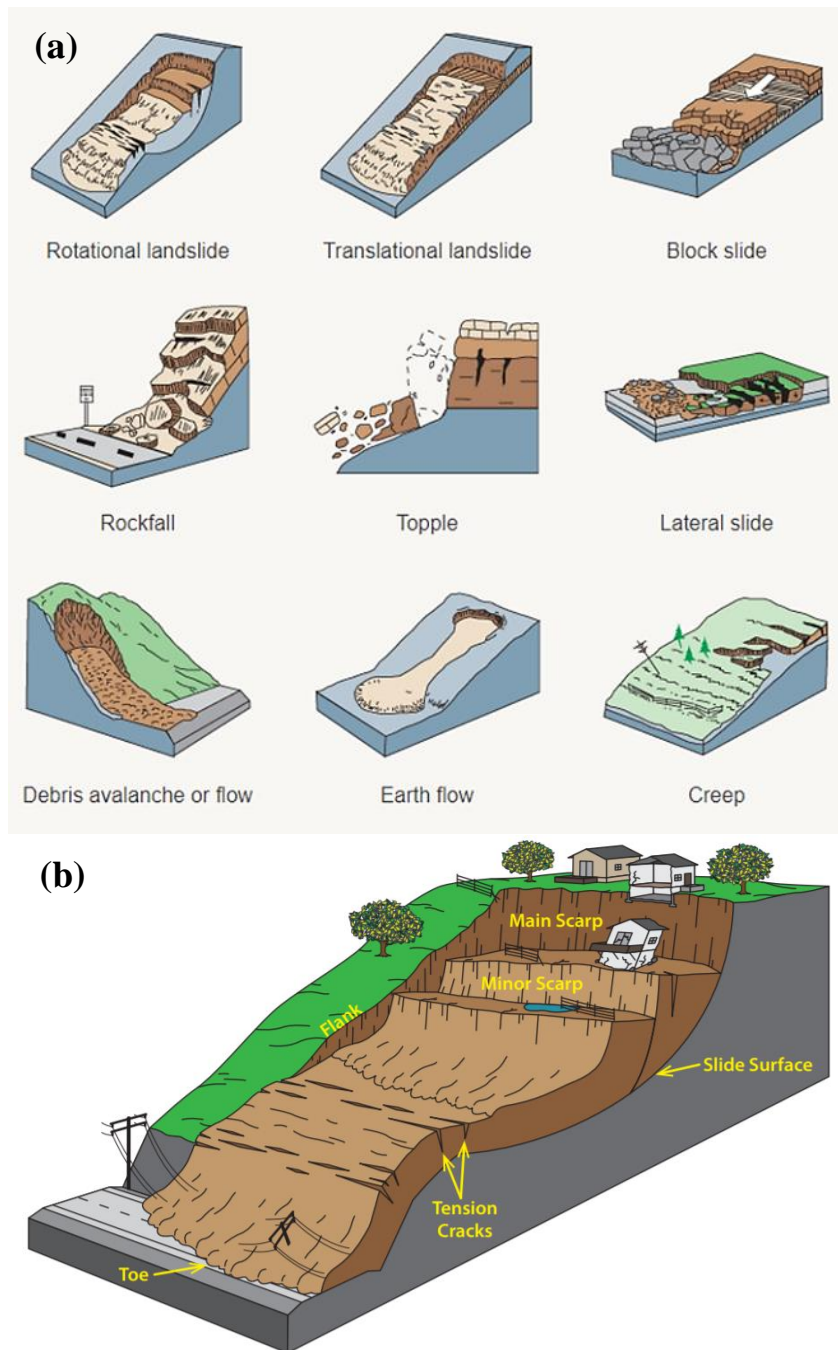


Figure 2: (a) Types of landslides based on behavior and speed in which material moves; (b) The geometry of a rotational landslide (Highland and Bobrowsky, 2008).

The types of landslides taken into consideration in the present study are slow-moving landslides with emphasis on slow rotational slides. Slow-moving landslides are common in areas underlain by or containing layers of weak, clay-rich soil and rock, and which receive high seasonal

precipitation (Lacroix et al., 2020). The acting forces generate a gradual movement where internal shear stress is sufficient to cause pre-failure progressive deformation. However, shear stress is not enough to cause an abrupt failure. Rotational slides have curved and concave rupture surfaces, called scarps (Figure 2b), in which (rotational) failures occur along axes parallel to the slope (Figure 2b). The optimum slope for the incidence of such types of landslides ranges from 20 to 40 degrees. The velocities of slow-moving landslides are usually extremely low but can range from less than 10 millimeters per year up to 100 meters per year (Highland and Bobrowsky, 2008; Lacroix et al., 2020). Rotational slides may initially exhibit a slow rate of movement, but can become rapid movement if the slides are exposed to events that can trigger a rapid displacement such as earthquakes or intense rainfall. In most cases, the interaction between the soft sedimentary layers along the slip surface lying underneath a strong cap rock and the triggering factors will aggravate the existing progressive slow deformation by accelerating failure rates (Highland and Bobrowsky, 2008; Hungr et al., 2014; Castro et al., 2020).

Several factors and events influence/trigger the occurrence of landslide phenomena though the nature and significance of the factors differ depending on the type of landslide. These include slope gradient, soil/geology, earthquake events, intense precipitation, and land use and land cover (Sarkar et al., 1995; Gökçeoglu and Aksoy, 1996; Hylland et al., 1997; Wachal and Hudak, 2000). For instance, land cover changes play a significant role in the stability of a slope because of the fact that vegetated areas tend to increase slope stability by reducing the erosion impact and absorbing soil moisture through roots. Areas with sparse vegetation are more prone to landslides than areas with dense vegetation (Gökçeoglu and Aksoy, 1996). The variation of seasonal events, particularly rainfall intensity, can also trigger landslides. Infiltration and direct interaction of rainwater, as well as the rising groundwater level with clay layers, especially high-plasticity and expansive (swelling) members, induce pore pressure changes that may reduce the normal force

(and hence the shear strength) and initiate slope failure (Wachal and Hudak, 2000; Hilley et al., 2004; Castro et al., 2020; Lacroix et al., 2020). In addition, other processes such as chemical or physical weathering, anthropogenic-led activities such as construction, leaking pipes, and poor drainage conditions can also contribute to slope failures. But it is worth mentioning here that most slope failures are triggered not by a single controlling factor or event but by combinations of many (Corominas et al., 2014; Lacroix et al., 2020; Shano et al., 2020). Assessing these factors can lead to a more comprehensive understanding of the nature of the processes and the complex interactions of the different factors that give rise to the formation of these hazards in any given area.

1.3. Geospatial Datasets and Techniques for Investigating Landslide Hazards

Most landslide occurrences and their rates of displacement are characteristically difficult to forecast and assess owing to their varying spatial scales, temporal pattern, distribution, mode of displacement, and the complex interactions between the material and controlling factors. This assertion particularly applies to certain types of landslides (e.g., rockfall, topples, debris flow) in which it is not practically feasible to forecast the possibility of occurrence of the landslides beforehand. This difficulty is mainly because the nonlinear time dependency nature of the landslides coupled with seasonal processes/events affects the displacement, resulting in an abrupt fast-velocity movement of the landslide material down a slope, which makes it difficult to detect and quantify the pre-failure displacements (Crosta et al., 2003; Lacroix et al., 2020). On the other hand, slow-moving landslide processes and interactions that can give rise to their occurrences can be modeled, and their potential incidence can be better forecasted with some degree of certainty because of their slow displacement rates. In such cases, the pre-failure displacement rates are considered main precursors that indicate the potential occurrence of landslides (Lacroix et al., 2018; Intrieri et al., 2019).

Several approaches and techniques have been proposed to help us understand the mechanisms of landslide processes, as well as methods to determine areas that are susceptible to landslide hazards (Shano et al., 2020). These techniques can broadly be grouped as landslide distribution (inventory) data analysis, heuristic (knowledge-based) terrain and susceptibility zoning, statistical methods, deterministic methods, and probabilistic methods (Aleotti and Chowdhury, 1999; Guzzetti et al., 1999; Kanungo et al., 2006; Corominas et al., 2014; Raghuvanshi et al., 2014, 2015; Ahmed, 2015; Reichenbach et al., 2018)

The growing capability of remote sensors on board satellite and aerial platforms and the free dispensation of publicly available data with varying spatial and temporal resolution acquired by the sensors are facilitating the use of the datasets and developed tools to investigate landslide susceptibility as well as hazard and risk zoning on different spatial and temporal scales (Guzzetti et al., 2012; Kirschbaum and Fukuoka, 2012). In addition, capabilities offered by Geographic Information Systems (GIS) techniques, which analyze and integrate various datasets representing the critical factors that directly or indirectly contribute to the formation of the landslide, are being used to identify areas that are susceptible to the incidence of the hazards (Chalkias et al., 2014).

1.3.1. GIS for Landslide Studies

One approach widely used to assess the potential vulnerability of local- to regional-scale-size areas to the threat of a landslide phenomenon is a landslide susceptibility map (LSM) generated using the heuristic approach. The map produced does not indicate the susceptibility of an area for a certain type of landslide but represents general susceptibility with respect to the different types of landslides. The heuristic method is the ideal choice for mapping landslide susceptibility for large areas where the landslide inventory data is limited and the analyst has a better knowledge of the landslide mechanisms of the area (Abella and Van Westen, 2008). LSM

products generated using the heuristic approach are nominally produced by integrating several parameters including the classification and compositions of geologic materials/soils, soil properties, steepness of the slope, and the occurrence of landslides in the past over the investigated area (Manzo et al., 2013; Ahmed, 2015; Arabameri et al., 2019; He et al., 2019). The generation of the LSM products using this approach can be facilitated through a GIS-based spatial Multi-criteria Decision Evaluation (MCE) method that integrates different variables considered as factors that control the likelihood of occurrence of landslide events over a given area (Feizizadeh and Blaschke, 2011). A distinct aspect of the GIS-based MCE methods, which generate qualitative results, in contrast with the other methods outlined above is that weights are assigned to the different variables with respect to their contribution to the incidence of the hazard. In most cases, weights are assigned arbitrarily based on the expert knowledge of the analyst of the project site. Alternatively, weights are determined following a hierarchy of decision-making procedures, called analytical hierarch process (AHP) method - a procedure in which sequences of pair-wise comparisons of the controlling factors in a matrix with scores depicting the relative importance of the factors against each other are assigned also based on the expert knowledge of the analyst (Yalcin, 2008; Ahmed, 2015; Roodposhti et al., 2019). For instance, El Jazouli et al. (2019) used a GIS-based spatial multicriteria approach to generate a LSM to identify landslide-prone areas in northern Morocco. Weights were assigned to eight parameters including land cover, lithology, distance to road, distance to fault, distance to drainage network, elevation, aspect, and slope gradient, and were integrated to produce the LSM. Though susceptibility maps can indicate areas where landslides could potentially occur, they cannot forecast when they will occur (Hylland et al., 1997; Young and Norby, 2009). Similarly, Wachal and Hudak (2000) assessed the susceptibility of Travis County, Texas, to landslide hazards. They assigned weights to several parameters including slope, geology, vegetation, and proximity to faults based on their perceived

significance for triggering a landslide. Though the result indicated some of the areas that are prone to the hazard, the quality of the generated product could be improved by incorporating datasets with improved spatial resolution and other potential parameters that could contribute to the triggering of a landslide phenomenon (e.g., rainfall intensity). Since LSM results indicate potential susceptibility from different types of slides as outlined earlier, it is difficult to determine active landslide processes that could lead to the occurrence of a landslide in the absence of ground deformation estimates that show current active processes (Lanari et al., 2004).

1.3.2. Remote Sensing for Landslide Studies

Remote sensing is a valuable tool to assess surface displacements that occurred post-landslide event or determine pre-failure displacement patterns that may eventually result in a complete slope failure. Various types of remote sensing datasets have been used to assess landslide development including space-borne Synthetic Aperture Radar (SAR), optical remote sensing, airborne, light detection and ranging (LiDAR), and ground-based SAR (Zhao and Lu, 2018; Wang et al., 2022).

Several studies have applied various analyses techniques on remote sensing datasets for mapping landslides or detecting pre-cursory landslide activities. In most cases, the remote sensing datasets are used as one of the inputs in the GIS-based landslide susceptibility models (discussed in section 1.3.1). For instance, most of the different kinds of MCE techniques incorporate remote sensing datasets directly or use derived products such as the Normalized Difference Vegetation Index (NDVI) calculated from optical remote sensing datasets (Pour and Hashim, 2017). Besides being used as input in MCE techniques, multi-temporal observations of a given site using the remote sensing datasets can be used to assess and monitor the susceptibility of a given site to landslide hazards. Lacroix et al. (2019) applied algorithms based on Landsat-8 images acquired

over the desert of southern Peru to study the internal processes affecting landslide kinematics, by quantifying the rates of slow-moving landslides over the area. On the other hand, SAR datasets are commonly used for quantifying displacement following a landslide event, detecting slow-moving landslides, and quantifying their pre-failure rates. These results are accomplished using different subclasses of a deformation analysis technique called Interferometric SAR (InSAR) (Scaioni et al., 2014; Martins et al., 2020; Solari et al., 2020).

CHAPTER TWO

STUDY AREA, OBJECTIVES, AND SIGNIFICANCE

2.1. The study area

The area of investigation in this study is the City of Austin and its surrounding areas (Figure 3). Austin is the state capital of the state of Texas, located in Travis County. In the past decade, the county saw a 24.4% population growth, and the metropolitan area of Austin is the most populated, with over 2 million inhabitants (United States Census Bureau, 2021). As noted in similar circumstances across the world where massive population growth and urbanization are driving communities to settle in natural hazard-prone areas (e.g., Klimeš and Rios Escobar, 2010), the high population growth rate of the Austin metropolitan has led to population expansion into areas that are susceptible to natural hazards (Bixler et al., 2021). Also, intense anthropogenic activities and changes are further compounding the increasing risk of natural hazards, especially those related to slope failures or land subsidence in some areas within the study area. For instance, a landslide occurred repeatedly (two incidents between May 2018 and May 2019) at the Pease Park (Austin) on a cliff that overlooks the Shoal Creek (identified by the green dot in Figure 3 and red boundary in Figure 4) causing considerable damage to public and private property.

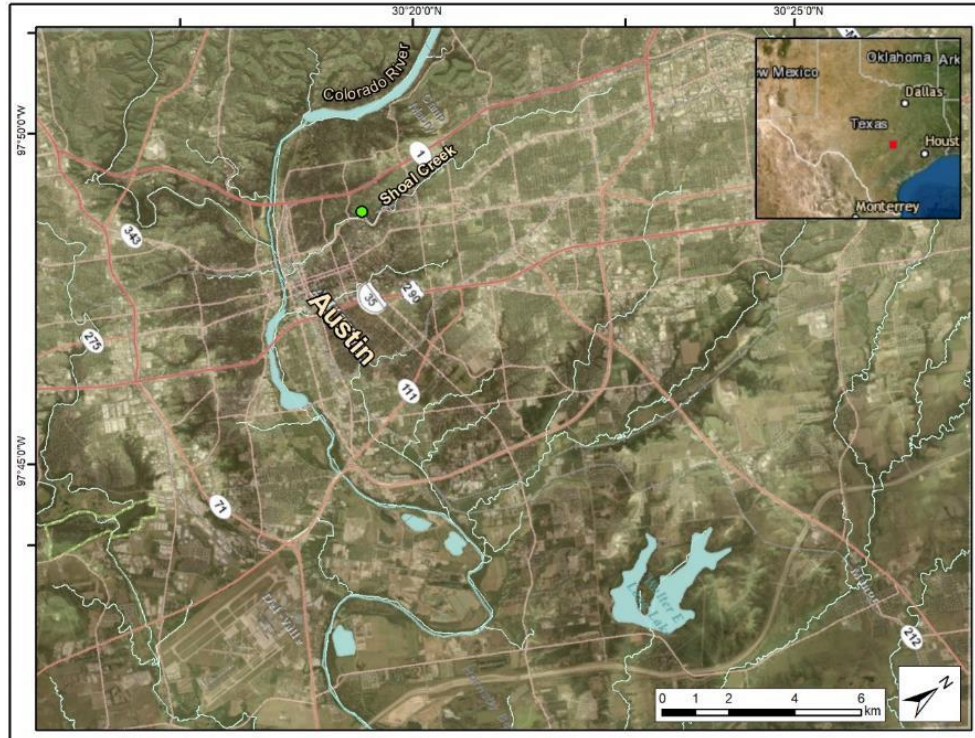


Figure 3: Location map of the study area. The green dot shows the location of the slope failure in the Pease Park which is located along the trail of the Shoal Creek. The inset map (top right) shows in red outline the location of Austin with respect to the state of Texas.

2.2. Statement of the problem

Landslides have been studied extensively as one of the destructive geological hazards. Though natural processes largely control their incidence, they can also be triggered by human activities resulting in enormous societal and economic impacts. Due to the nature and the way some landslide types occur, such as slow-moving slides, it is possible to detect and model the dynamics of the pre-failure processes and their rates that eventually lead to slope failure with some degree of certainty (Lacroix et al., 2020). As stated in section 2.1, some areas in Austin city, such as the Pease Park along the Shoal Creek (Figures 3 and 4), have experienced slope failure events (May 2018 and May 2019) that were preceded by slow pre-failure deformation processes and rates (Hammons, 2018). Figure 4 shows images acquired over Pease Park preceding and following the first landslide incident (2018) that occurred at Pease Park along Shoal Creek. Detecting and

mapping susceptible areas to this kind of slow-movement landslides, as well as understanding the triggering factors that lead to those processes, is helpful in land use planning to reduce the risks stemming from these kinds of natural hazards.

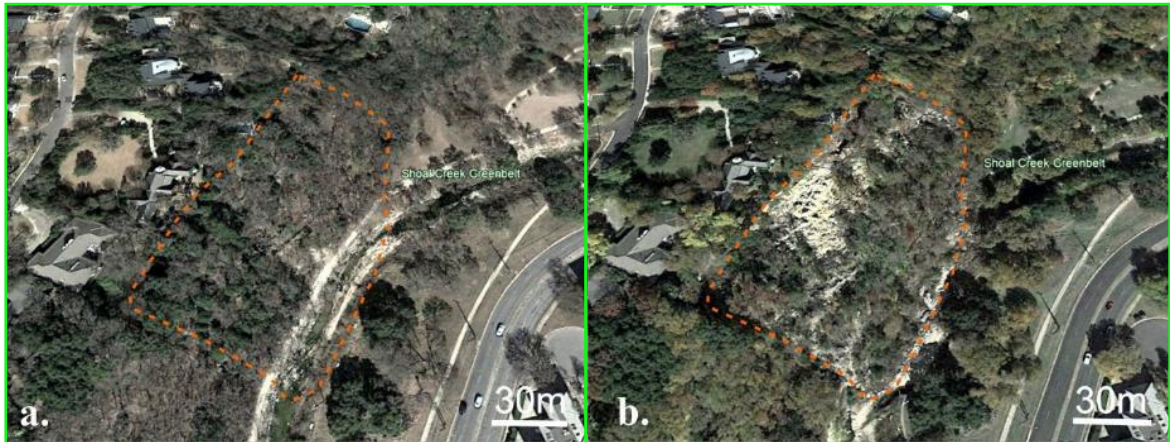


Figure 4: Google Earth images of the Pease Park located along the Shoal Creek before (a) and after (b) the first slope failure event in 2018.

2.3. Research Questions, Objectives, and Significance

The general scope of this study is to accomplish a functional integration of multiple datasets coupled with field-based validation procedures for the following key objectives:

- Identify areas that are susceptible to a landslide hazard in Austin City and its surroundings.
- Describe the factors that control the occurrence of the hazard and assess the potential relationship between the controlling factors. Deformation pattern and related information observed on existing slides, such as size and geometry, will be used to model the mode of formation of potential landslides over the study area.
- Distinguish slow-moving landslides and quantify their rate of displacements that can be used as input for forecasting their occurrences.

To attain the objectives of the research, the following research questions were addressed:

- What is the spatial distribution of the landslide susceptibility categories in the study area?
- What are the controlling factors that may influence the development of slope failures?
- What is the drawback of traditional LSM models with respect to identifying slow-moving slides?
- How are slow-moving slides determined? What sets of criteria are used to discern slow-moving slides from fast-moving ones? What precursors can be used as indirect indicators to discern slow-moving slides in the field?

Fulfilling the objectives and answering the research questions of the study will highlight the importance of mapping landslides as geological hazards in the study area. It provides insights into the processes that give rise to landslide incidences and the roles of the different triggering factors in influencing their formation, and the evolution of slow-moving landslides from pre-failure inception to sudden prompt failure. The findings of this study could be used to develop landslide early warning system as well as provide valuable information to the community and policymakers for land use planning and other development endeavors. In addition, the approaches and dataset selection and integration demonstrated in this study can be used to investigate similar problems in other areas with similar geological and environmental settings.

CHAPTER THREE

GEOLOGIC, HYDROLOGIC, AND CLIMATIC SETTINGS

3.1. Geography, Climate, and Hydrology

The study area is located in south-central Texas (Figure 3). The elevation ranges from 110 meters to more than 300 meters above sea level. The dominant geomorphology of the study area includes the Balcones Escarpment - a Faultline scarp which is the surface expression of the Balcones Fault Zone (BFZ). This zone separates two dominant landscapes belonging to different topographic regions prevailing in the area. The eastern part is characterized by flatlands and terraces of the Colorado River, with heavy clay and loam soils, which physiographically belongs to the Gulf Coastal Plain. On the other hand, the western part of the study area is characterized by its more rugged hills comprised of deeply dissected limestone with karst topography. These western hills represent the easternmost expressions of the Edwards Plateau (Hill and Vaughan, 1902; Baker, 1975; Barker et al., 1994).

The climate of the study area is described as humid subtropical climate with long moderately hot summers and mild winters. Records of the National Weather Service show that the mean annual temperature is 20°C. The area receives a moderate amount of precipitation, with average annual precipitation values ranging from 812 millimeters to 914 millimeters, during two rainfall seasons: spring (April – June) and fall (September – October) (Brune et al., 1983; Patil et al., 2021; Simmons et al., 2008; Prudent et al., 2016).

The study area falls within the Colorado River Basin, where the network of streams drains from the northern hills, western, and eastern areas to the main hydrological feature of the study area, the Colorado River (Figure 3). Three artificial lakes: Travis Lake, Austin Lake, and Ladybird

Lake built along the Colorado River influence on the area of interest. The Mansfield Dam, Tom Miller Dam, and Longhorn Dam help control the river waterflow to the lakes. (Mays, 1991).

3.2. Geological Framework

3.2.1. Regional Geology

Travis County is divided into two geological provinces dissected by the BFZ. An epeirogenic uplift as a result of extensional faulting and fracturing in the Trans-Pecos region created the western province during the late Oligocene and early Miocene. This process is also believed to have created the BFZ. The main geological formations of the Edwards Plateau include Lower Cretaceous limestone and marl units deposited during a Cretaceous transgressive period. The Edwards Plateau is considered the hilly portion of the county, representing hills with relatively steep slopes and thin soils overlying limestone bedrock (Ferring, 2007; Housh, 2007; Clark et al., 2020).

The BFZ marks the transition between the Edwards Plateau to the west and the Gulf Coastal Plain to the east (Figure 5). The late Oligocene to early Miocene-aged BFZ consists of an echelon network of normal faults dipping towards the southeast (Coastal Plain) and striking northeast-southwest (Maclay and Small, 1983; Weeks, 1945). The Cenozoic Gulf Coastal Plain province was developed during a prolonged period of marine regression. Organic-rich clay sediments deposited on a continental shelf and now form the most fertile soils of this province (Ferring, 2007).

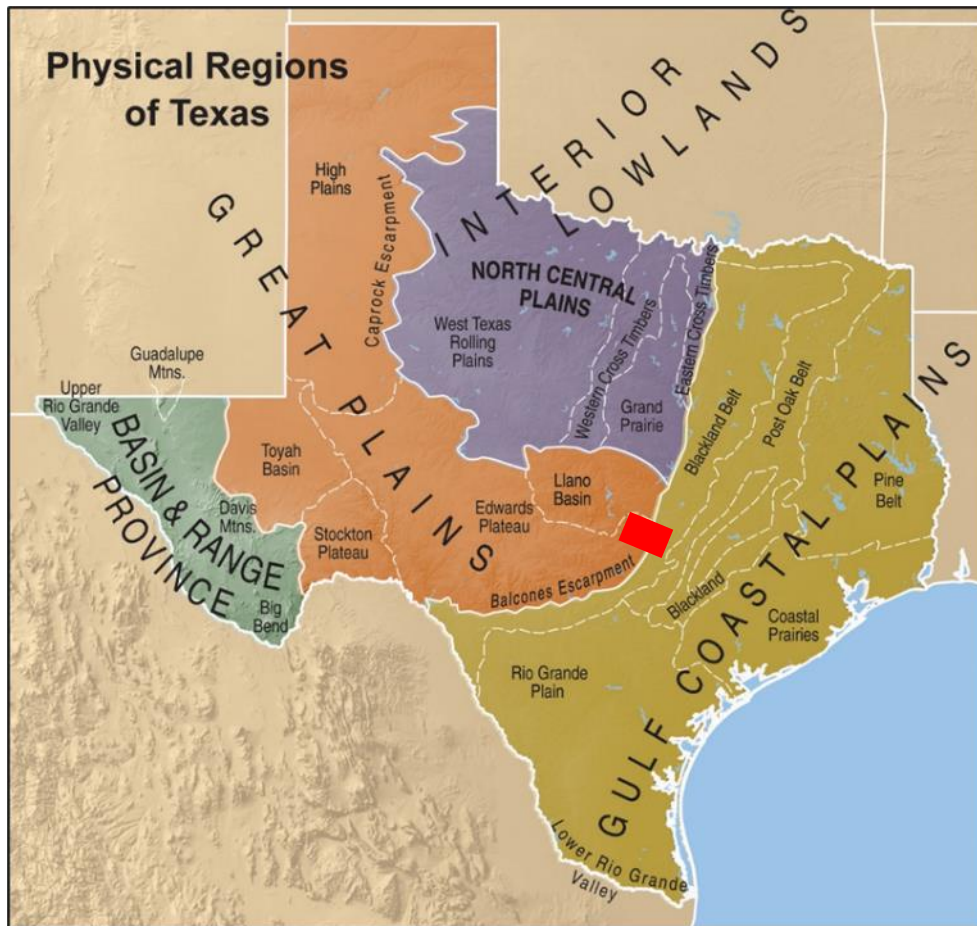


Figure 5: Travis County (red box) reference location in physical regions of Texas (Butler, 2021).

3.2.2. Local Geology

Sedimentary rocks that range in age from Early to Late Cretaceous dominates the geology of the study area (Figure 6). Other geological units prevailing in the area include igneous rocks, and Quaternary unconsolidated sediments (terrace and alluvium deposits) derived from marine sedimentary rocks, and igneous rocks transported to the study area by the Colorado River and its tributaries (Figure 6). The Early Cretaceous sedimentary rocks, classified under the Comanche Series, mainly consist of limestone formations comprising alternating beds of hard and soft limestone layers interbedded with beds of marly/clayey layers. This series consists of the Trinity Group, which includes the Travis Peak and Glen Rose formations, Washita Group represented by the Georgetown Limestone, Del Rio Clay, and Buda Limestone formations, and the Fredericksburg

Group consisting of the Edwards Limestone and Walnut Formation (Figure 6). The Late Cretaceous units are part of the Gulf Series class, which includes the Eagle Ford Group consisting of the Eagle Ford Formation, Austin Group; Taylor Group comprising the Ozan Formation, Pecan Gap Chalk, and the Navarro Group. These formations are spatially distributed across the study area though units of the Navarro Group are mainly observed in the northern part of the study area (Figure 6). The main lithological units of the Gulf series include marl, marly (laminated) clays, shales, chalk (Austin), and calcareous shale with thin interbeds of silty and sandy limestone. As indicated earlier, the northeast-southwest trending BFZ is the primary structural zone in the study area. This zone is spatially concentrated around the western boundary of the study area (Figure 6) (Hill and Vaughan, 1902; Adkins and Lozo, 1951; Young, 1977; Barnes et al., 1981; Brune and Duffin, 1983; Wachal and Hudak, 2000; Clark et al., 2016).

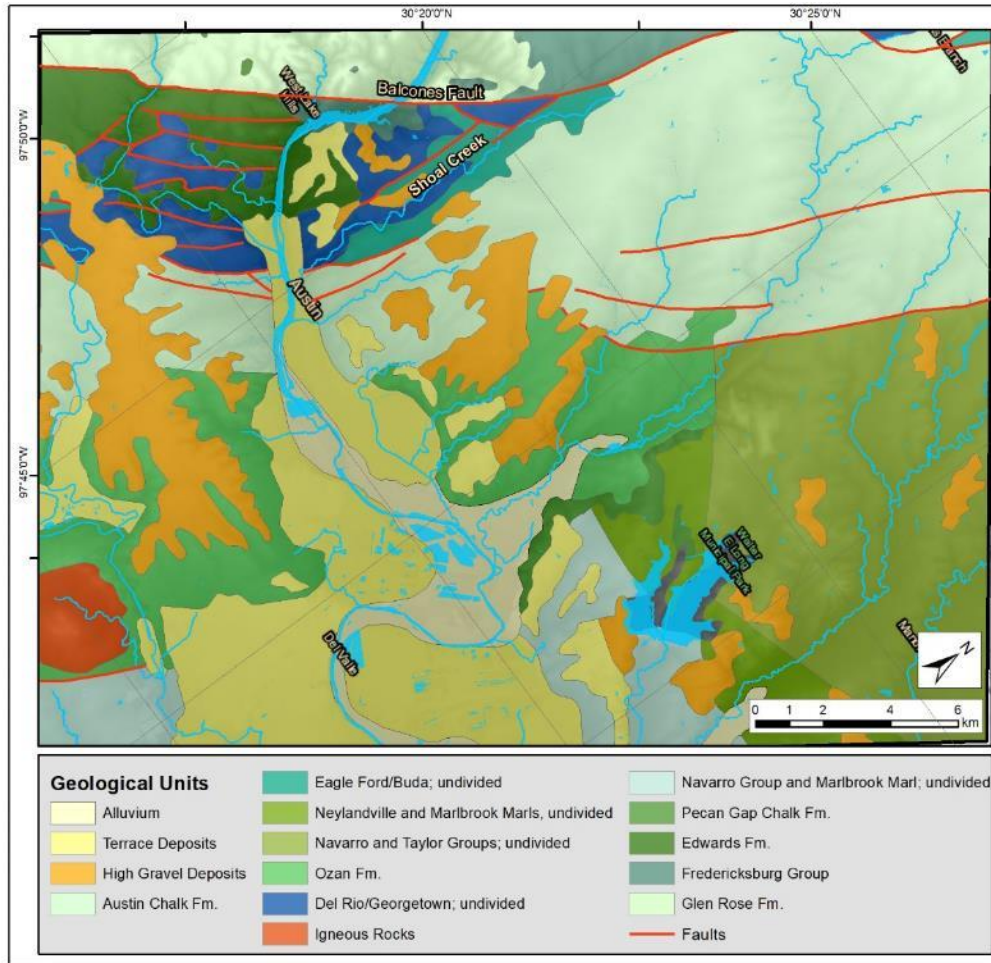


Figure 6: Spatial distribution of the geological units and faults in the study area retrieved from the Geologic Atlas of Texas: Austin Sheet (Barnes, V.E. et al., 1981).

This study focuses on the Del Rio Clay Formation and Buda Formation. Both formations are weak and the dominant formations in the Pease Park located along the Shoal Creek (Figure 7), which has repeatedly experienced landslide events. The Del Rio is mainly a laminated, calcareous, and gypsiferous clay and claystone with locally present pyrite (Hill, 1977). The clay exhibits a shrink-swell behavior and dominantly contains montmorillonite and kaolinite, and minor amounts of illite (Garner et al., 1976; Young, 1977). Plummer (1949) stated that up to 12 meters of Del Rio clay crop out on the west bank of Shoal Creek. Hill and Vaughan (1902) also stated that the Del Rio Clay is typically found along Shoal Creek, where the thickness ranges from 24 to 30 m. The

Del Rio overlies the limestones of the Georgetown Formation (Early Cretaceous) and underlies the Buda Limestone (Late Cretaceous) with unconformable contact (Bullard, 1953; Hill, 1977) (Figure 8).



Figure 7: Massive Block of the Buda Formation on top of the Del Rio Formation (part of the material from the slope failure incident on Pease Park).

Hill (1977) described the Buda Formation, termed the “Shoal Creek limestone in early literature (Hill and Vaughan, 1902), as a fine-grained, bioclastic, commonly glauconitic, pyritiferous, hard, massive limestone (Figure 7). The Buda limestone crops out intermittently in areas throughout the BFZ (Figure 6). It overlies the Del Rio Formation (Figure 7) and a thin clay layer of the Eagle Ford Formation overlays it. Overall, the Buda Formation is very thin having a maximum thickness of 14 meters (Hill and Vaughan, 1902) (Figure 8).

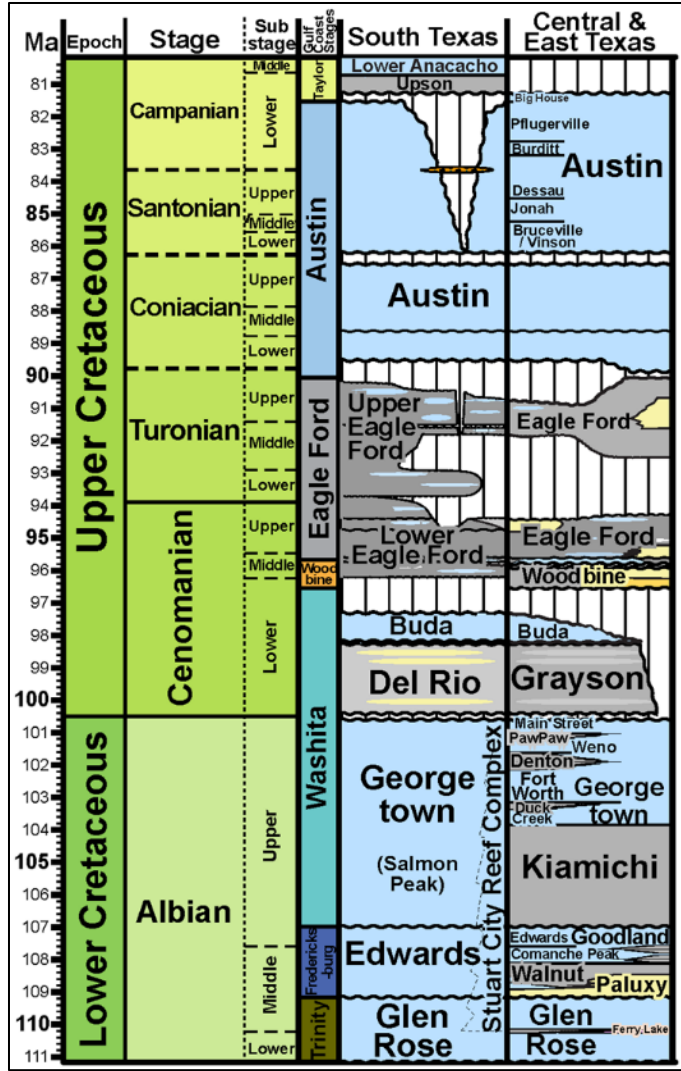


Figure 8: Diagram of Cretaceous lithologic units and zonal stages of formations in Texas. Note that the Buda Formation overlies the Del Rio Formation (taken from R. A. Denne, 2022, unpublished data).

CHAPTER FOUR

DATA AND METHODS

4.1. Overview

An integrated study approach comprising several datasets and techniques was used to investigate each of the study objectives. Initially, the incorporation of several datasets/parameters that constrain the occurrence of the events identified landslide-prone areas. A close investigation of the landslide events (May 2018 and May 2019) that occurred in the Pease Park of the Shoal Creek area was undertaken to test the accuracy and reliability of datasets obtained from different sources. The incidence of the event was also used to test the validity of the hypothesized mechanism of formation of landslides in the study area that this research presents. The result obtained using the susceptibility mapping procedure was not restricted to mapping areas prone to slow-moving slides, but also includes the susceptibility to fall and other types of fast-moving slides. Hence, a secondary approach that isolates and detects slow-moving slides whose occurrences can be forecasted based on their trajectories and rates of displacement is required.

An InSAR technique was applied on remote sensing datasets to supplement the result from the susceptibility mapping. This technique becomes particularly useful in isolating areas experiencing slow displacement. The presence of several limitations that could affect the accuracy of the results obtained using the InSAR method dictates the need for the integration of auxiliary datasets to calibrate and validate the analysis result. In addition, other ancillary datasets, such as soil textural analysis results, as well as the 3D model of the landslide at the Pease Park generated by using the Structure from Motion (SfM) algorithm applied on aerial

photographs acquired by Unmanned Aerial Systems (UAS), provided for further validation and interpretation of the results.

A detailed description of the datasets and approaches employed in each of the above-stated procedures are outlined below.

4.2. Landslide Susceptibility Mapping (LSM)

In this study, the (heuristic) MCE method was employed to qualitatively assess the landslide susceptibility of the study site. Each of the controlling factors presumed to influence the incidence of the landslide over the study area categorized into different classes of susceptibility (Ayalew et al., 2004), followed by the assignment of weights to each variable based on their perceived level of relative importance (Kritikos and Davies, 2011). The Weighted Linear Combination (WLC) model (Malczewski, 2000) was used to combine all weights and variables and generate a landslide susceptibility index (LSI) indicating the level of susceptibility in different parts of the study area for the landslide hazard.

4.2.1. Controlling Factors

Six potential landslide causative factors were identified in this study, and conventional thematic data representing these factors were used for data analysis: slope gradient, land cover, geology and structures, drainage network, and precipitation. These controlling factors were considered based on the local conditions and the potential factors that led to slope failure at the (Pease Park) Shoal Creek site. The datasets representing the controlling factors were acquired in varying spatial resolutions and extents. The initial step (pre-processing) of assessing the individual controlling factors was resampling the spatial resolution of all the individual datasets to the resolution of the fine-scale thematic dataset and clipping them to the extent of the study site. This step is followed by the classification of the thematic layers into different categories. Analysis tools

in Environmental Systems Research Institute (ESRI)'s ArcGIS software were used for the pre-processing of the datasets, analyses of the individual controlling factors, and the final susceptibility product generation.

i. Slope Gradient

The change in the slope gradient across the study area, given in degrees, is considered in this study as one of the controlling factors for the incidence of a landslide event over the study site. The slope map for the study site was created by using Digital Elevation Model (DEM) data, a digital representation of the elevation representing the topography in an area and stored in a raster format. The DEM data for the slope analysis was acquired by the Light Detection and Ranging (LIDAR) sensors with a pixel size resolution of 1 meter. The dataset was obtained from the Texas Natural Resources Information System (TNRIS) online data distribution platform (<https://data.tnris.org>). The slope tool in the ArcGIS software was used to calculate the slope as the maximum rate of change in vertical value between each pixel and its immediate neighbors. The ranges of values obtained were then classified into four categories based on the steepness or flatness of the slope angles.

ii. Land Cover

The land cover information was included in this study as an important causative factor that controls the incidence of landslide events. Several landslide susceptibility analyses have indicated that barren lands or areas with low vegetation density are prone to erosion and slope failure. Mechanical reinforcement of soils through plant roots helps stabilize slopes, though the effect of the strength on the slope stability varies depending on the vegetation type. Man-made activities, such as road and other construction work, or natural processes that change the land cover conditions from dense vegetation to light vegetation, also have a direct effect on slope stability

(Stokes et al., 2008; Mao et al., 2014; Reichenbach et al., 2014; Firomsa and Abay, 2019; Liu et al., 2021). The land cover data used for this study, the 2019 National Land Cover Database (NLCD), was developed by the United States Geological Survey (USGS). The NLCD was developed based on Landsat 8 imagery and has a spatial resolution of 30 m (Pourpeikari et al., 2022). The land cover data was resampled to obtain a 1-meter spatial resolution for compatibility with the slope gradient and other datasets.

iii. Local Geology and Geological Structures

The geology/soil composition strongly affects slope stability (Çellek, 2020). Hence, specific attention was given to the geology and soil composition of the area, as the strength, cohesion, and permeability of rocks and soils may vary depending on the variability of the lithological composition of the materials in the area. Generally, areas with a higher percentage of unconsolidated material have less cohesion developing less shear strength than consolidated rocks. In addition, the presence of weak materials with clay-rich zones/layers in the lithological units also creates favorable settings for initiating landslides, particularly slow-moving slides. The clay-rich layers in these instances act as sliding surfaces or failure zones (Lacroix et al., 2020).

The distance to faults and other geological structures (of an area) plays a key role in the stability of a slope. Psomiadis et al. (2020) stated that with increasing distance from faults and other geological structures, there is a reduction in the probability of landslide events happening. The effect of faults and other geological structures on landslide events is two-fold: (1) stress buildup in active geological structures induces slope instability by disturbing and weakening the cohesion of the geologic material leading to reduced shear strength (Wachal and Hudak, 2000; Abedini and Tulabi, 2018; Lacroix et al., 2020), and (2) the geological structures may act as

conduits to transfer water from the surface to layers at depth, whose interaction with water may initiate processes that ultimately result in slope failure (Psomiadis et al., 2020).

The lithological and geologic structure data of the study area were obtained from a 1:250,000 map downloaded from the TNRIS data distribution platform (<https://data.tnr.org>). Complementary mapping of geological structures over the study area was undertaken by using SAR datasets. The purpose of the delineation exercise was to extend the susceptibility mapping to areas where geological structures were not defined/identified using conventional methods in earlier mapping exercises/studies. The methodology outlined by Tagnon et al. (2020) for evaluating linear structures associated with faults and fractures was adopted for delineating the features. In this method (Tagnon et al., 2020), the geological features are delineated manually by observing the change in the backscatter intensity of SAR images acquired over the area after applying adaptive filters. The use of the filters allows to remove speckle and other noises and increase the sharpness and details of the SAR images to highlight lineaments that could be interpreted as fractures or faults. Sentinel-1 (level-1) datasets were processed using the open-source software Sentinel Application Platform (SNAP) to delineate the tectonic features in the study area by using the approach outlined earlier. The high-spatial resolution DEM data (1-m resolution) of the study area was integrated in this procedure to further supplement and refine the SAR-based structural mapping technique.

Once the lineaments were identified, the existing structural map became a tool to visually compare if there is a spatial correspondence with the patterns identified as fractures using the SAR-based technique. The premise here is that, if there is a spatial correspondence between the existing faults in both maps (structures from the geological map and the SAR-derived structural map), it corroborates the reliability of the method, validating the accuracy of the mapped structures in other

parts of the study area. Finally, buffer zones generated using incremental distances away from the geological features were used to assess the impact of the features with respect to contributing to triggering landslide events. Generally, areas proximal to geological faults constitute more fractured and unconsolidated materials and are thought to be more susceptible to slope failure.

iv. Drainage Network and Precipitation Data

In this study, the distance to the drainage network and precipitation were also considered as triggering factors for a landslide incidence. Both factors can have a profound impact on the effective stress state in earth materials influencing hillslope stability (Iverson and Major, 1987; Terzaghi et al., 1996). This impact is accomplished either by raising the pore pressure on the failure plane through direct infiltration of water or raising the groundwater levels and interaction with weaker units at depth, or through direct aggressive weathering effect of the waterways/drainage networks on the slopes. Both processes reduce the effective normal stress and frictional resistance (Iverson and Major, 1987; Tong and Schmidt, 2016; Abedini and Tulabi, 2018; Castro et al., 2020). Areas with high precipitation rates, when coupled with other factors that facilitate the occurrence of a landslide event are more vulnerable to landslide occurrence. The spatial distribution of drainage networks and their distances from landslide-prone areas and the incidence of landslide events have an inverse relationship – that is, increases in the distance of the drainage networks from landslide-prone localities underlain by weak units decreases the possibility of a direct effect on the slopes or infiltration and interaction of water with the materials at depth and, subsequently, the potential for a landslide incidence decreases (Dai et al., 2001; Yilmaz et al., 2012; Firomsa and Abay, 2019).

The drainage network data of the study area was extracted from the same 1-meter spatial resolution DEM that was used for the slope gradient analysis. The hydrology tool in the ArcGIS

software was used to extract the drainage network from the DEM. The influence of the spatial distribution of the drainage networks in initiating the occurrence of landslides over parts of the study area was assessed by generating a series of buffer zones indicating the proximity of the areas with respect to the drainage networks. Additionally, long-term daily rainfall datasets (1980–2019) retrieved from the Parameter-elevation Regressions on Independent Slopes Model (PRISM) Climate Group (Daly, 2006) were integrated in the analysis. The spatial resolution of the PRISM gridded data is 4 km. The entire extent of the study area was covered by four grid cells. The daily precipitation values for each of the grid cells were converted into yearly average (annual mean) precipitation values. The results of the mean annual precipitation value for each grid cell center were used to generate a raster surface that takes the effect of the surrounding grid centers/precipitation values on each of the individual grid center values into account using the Inverse distance weighted (IDW) interpolation tool in the ArcGIS software.

4.2.2. Landslide Susceptibility Index

Using the WLC technique outlined earlier, an index of susceptibility was calculated by integrating the raster-based thematic data representing the various landslide controlling factors and the assigned weights described above in a GIS setting. Each of the controlling factors was clustered into four categories/classes and rated with values ranging from 1 to 4 assigned to each of the categories. A value of 1 indicated low significance of the condition within each of the controlling factors for initiating a landslide hazard, whereas a value of 4 represented a higher influence of the conditions stated in the category for the occurrence of slope failures. Besides rating the classes, each controlling factor was assigned a weight based on the perceived level of importance of the controlling factor in initiating a landslide hazard. The susceptibility index is calculated using the WLC technique shown in equation (1) below (Rahim et al., 2018):

$$LSI = \sum_{i=0}^n F_i * W_i \text{ (Equation 1)}$$

Where LSI is the landslide susceptibility index, F is the rating value of the individual controlling factors, and W is the weight assigned to each of the controlling factors.

4.3. Detecting and Quantifying Slow-Moving Landslide

4.3.1. SAR Datasets

In this study, techniques applied on multi-temporal SAR images were used to detect and quantify slow-moving slides. SAR datasets are acquired by side-looking radar systems, which emit electromagnetic signals in various microwave wavelength ranges (bands) (Fitch, 2012; Moreira et al., 2013). Some of the operational bands of past and current sensors onboard satellite and aerial platforms are shown in Table 1. SAR systems are classified as active remote sensing tools because of their operational capabilities to generate their own energy, which gives them the ability to acquire Earth observations during day and night. In addition, SAR signals can propagate through dense cloud and vegetation cover conditions to image the surface depending on the type of band used by the sensor (Blumberg, 1998; Garello, 2010; Helz, 2021).

Table 1: Most commonly used microwave bands in past and current SAR sensors with correlated frequency, wavelength, and known applications (modified from <https://www.earthdata.nasa.gov/>).

Band	Frequency	Wavelength	Typical Application
X	8–12 GHz	3.8–2.4 cm	High resolution SAR (urban monitoring, ice and snow, little penetration into vegetation cover; fast coherence decay in vegetated areas)
C	4–8 GHz	7.5–3.8 cm	SAR Workhorse (global mapping; change detection; monitoring of areas with low to moderate penetration; higher coherence); ice, ocean maritime navigation
S	2–4 GHz	15–7.5 cm	Little but increasing use for SAR-based Earth observation; agriculture monitoring
L	1–2 GHz	30–15 cm	Medium resolution SAR (geophysical monitoring; biomass and vegetation mapping; high penetration, InSAR)
P	0.3–1 GHz	100–30 cm	Biomass, vegetation mapping and assessment.

The surveillance geometry of a side-looking radar on a spaceborne system moves along a path with a certain velocity at altitude h , sending a short microwave pulse to the Earth's surface through its antenna attached to the platform to transmit and receive the electromagnetic signals (see Figure 9). The pulse length that instantaneously illuminates the area on the ground is generally known as the antenna footprint (as denoted by the gray area in Figure 9). The spatial separation of two acquisition spots of the satellite at different times is known as the baseline. The perpendicular projection of the spatial baseline (from the first satellite position) to the Line of Sight (LOS) of the second position is called the perpendicular baseline (Hanssen, 2001; Lu et al., 2007; Prati et al., 2010; Gebremichael et al., 2018).

The radar signals bouncing back from target surfaces in response to the initial transmission, called backscatter, are recorded by the sensor in the form of amplitude (A) and phase (\emptyset) of received signals as a function of time (Cutrona, 1990). The amplitude shows the strength of the return signal, while the phase component measures the relative distance between the sensor and the target (sensor-to-target distance) (Moreira et al., 2013). The strength of the backscattered signal collected at the sensor varies as a function of the physical and electrical properties of the target surface. These properties include the geometry, roughness, and dielectric properties of the target surface. In addition, radar system properties such as variation in wavelength also affect the properties of the backscatter signal (Walker et al., 2004; Sadeh et al., 2018). The flight path of the satellite or aircraft carrying the SAR sensor onboard is known as along-track or *azimuth* direction, and the (slant) *range* is the direction that is perpendicular to the azimuth direction (Figure 9) (Bamler and Hartl, 1998; Oliver and Quegan, 2004; Moreira et al., 2013).

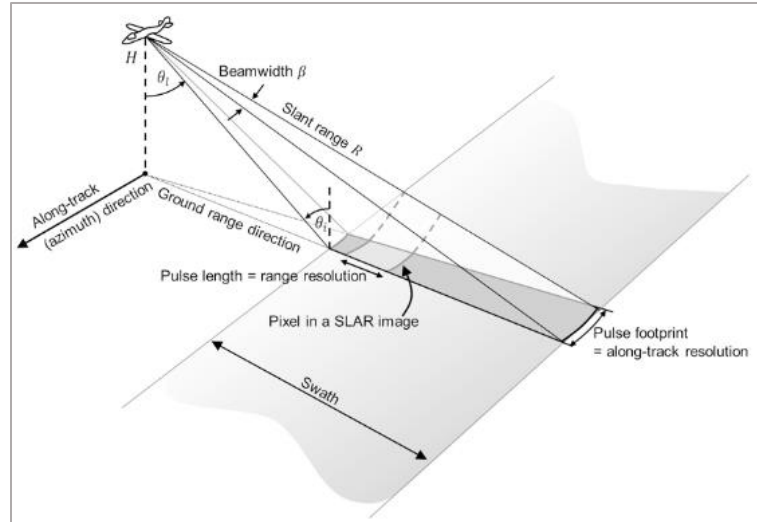


Figure 9: SAR image acquisition geometry. The radar sensor flights along the azimuth direction at an altitude H observing the Earth's surface at an oblique look angle θ_t . The illuminated footprint size is based on the antenna Beam width β , and the distance from the sensor to the ground R (Flores-Anderson et al., 2019).

Fifty-three Interferometric Wide swath (IW) mode level-1 Single Look Complex (SLC) SAR imagery (March 2015–January 2021) acquired by the Sentinel-1 mission (Table 2), operated by the European Space Agency (ESA), were used in this study for quantifying subtle rates of deformation emanating from slow-moving slides. The images were acquired along ascending flight path 107 and frame 93 (Table 2). The images were downloaded from the National Aeronautics and Space Administration (NASA) Alaska Satellite Facility (ASF) SAR Distributed Active Archive Center (DAAC) (<https://asf.alaska.edu/>). The Sentinel-1 mission comprises the Sentinel-1A and 1B satellites that were launched in 2014 and 2016, respectively. At the time of writing (April 2022), this mission remains the only source of open-access SAR data. The Sentinel-1 mission operates in the C-band (5.6 cm wavelength), having an operational mode of wide swath with a 250 km swath at 5 m by 20 m spatial resolution, high geometric and radiometric resolution, and short revisit time (6–12 days) (Crosetto et al., 2016; Lu et al., 2018).

Table 2: Sentinel-1 scenes used in this study that were acquired along orbital track 107. The super reference scene (2019-02-25), which all the other images were aligned to (a procedure called coregistration – discussed below) is shown in a dark gray background.

Time-Position Plot	Acquisition Date
0	20150318
1	20150821
2	20170424
3	20170518
4	20170611
5	20170717
6	20170822
7	20170915
8	20171114
9	20171208
10	20180101
11	20180125
12	20180218
13	20180314
14	20180407
15	20180501
16	20180525
17	20180712
18	20180805
19	20180910
20	20181004
21	20181028
22	20181121
23	20181227
24	20190120
25	20190225
26	20190321
27	20190414
28	20190508
29	20190601
30	20190625
31	20190719
32	20190812
33	20190905
34	20190929
35	20191023
36	20191116
37	20191210

Time-Position Plot	Acquisition Date
38	20200103
39	20200127
40	20200315
41	20200408
42	20200502
43	20200526
44	20200619
45	20200725
46	20200818
47	20200911
48	20201005
49	20201029
50	20201122
51	20201228
52	20210121

4.3.2. Surface Deformation Estimation using InSAR

A sub-class of the InSAR technique (discussed below) using the Sentinel-1 SAR datasets as input was used in this study to estimate the surface deformation rates resulting from the slow-rate landslide displacements. InSAR technique can detect and measure large/regional-scale vertical surface deformation and change processes at a spatial resolution of tens-of-meters (Massonnet and Feigl, 1998; Lu et al., 2007). Displacement rates are estimated based on the relative movement of the targets with respect to the satellite/sensor. Due to the high accuracy and fine-scale displacement measuring capabilities, these techniques are widely used for detecting slow-moving landslides and quantifying the ground displacement velocities of the slides. InSAR techniques require the phase information stored from the radar imaging to assess the distance between the sensor and the surface or target. When two radar images of the same target are acquired at different times, and from different orbit positions, the respective electromagnetic waves at a given point interact (Figure 10). This interaction is a phenomenon known as interference, where the waves will either be combined, resulting in their intensification, or they will cancel each other out. InSAR capitalizes on the interference information resulting from the interaction of the two waves to measure distance from

the satellite antenna to ground surface targets (Lu et al., 2007; Prati et al., 2010; Helz, 2021). The resulting product in which the interferences are depicted as a series of fringes/pattern is called an interferogram and the method, suited for quantifying large-scale displacements resulting from major processes that induce massive surface deformation, such as large earthquakes, is called Differential Interferometric Synthetic Aperture Radar (DInSAR) (Bamler and Hartl, 1998; Blanco-Sánchez et al., 2008; Wiecek and Snyder, 2009; Zhou et al., 2009; Flores-Anderson et al., 2019)

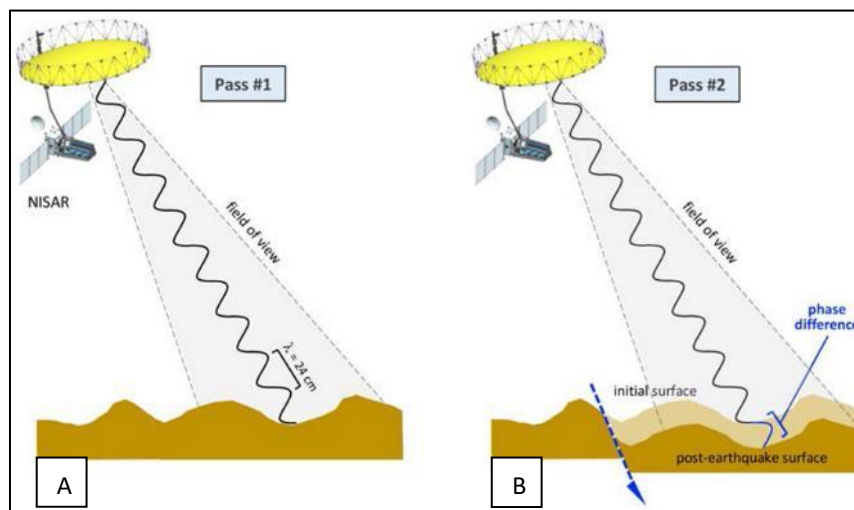


Figure 10: InSAR deformation geometry. In A (Pass/flight 1), a ground surface is imaged. In B (Pass 2), the satellite passes over the same area. If a ground deformation incident (e.g., from an earthquake) occurs between flights, the change in phase, which is proportional to the ground deformation between passes along the radar beam's Line-of-Sight (LOS) direction, is used to calculate the rate of displacement (NASA, 2020).

The interferogram generation requires multiple observations using the same sensor through complex multiplication to measure the similarity of two images, known as *interferometric correlation*, or *coherence*. Coherence, values ranging from 0 to 1, is a measure of the quality of the interferogram formed from each pair of coregistered complex images. The value of coherence decreases with increasing system noise, if there are changes in the scattering properties of the target surface, and increasing spatial and temporal baselines (Zebker and Villasenor, 1992; Zhou et al., 2009). Key processing steps of the DInSAR technique described by Okeke, (2006) include:

- **Pre-processing** - includes data search and selection as key steps to obtain reliable and good quality ground displacement results. Several factors influence the accuracy and reliability of the deformation result, such as: SAR data availability, spatial and temporal baselines between the acquisitions, and the sensor's band of operation.

- **Coregistration** - refers to the process of superimposing two or more SAR images with an equivalent acquisition geometry to align the samples for phase differencing. The primary (reference) and secondary SAR images will be compared to make sure that pixels in the corresponding images represent similar ground target.

- **Interferogram generation** - is achieved through the cross-multiplication of the primary image with the complex conjugate of the secondary image. The recorded amplitude of both images is multiplied whereas phase values are differenced forming the interferogram (Pepe and Calò, 2017). The resulting complex interferogram (\emptyset_{comp}) comprises several components as shown below:

$$\emptyset_{comp} = \emptyset_{flat} + \emptyset_{topo} + \emptyset_{disp} + \emptyset_{atm} + \emptyset_{orbit} + \emptyset_{noise} \quad (\text{Equation 2}),$$

where \emptyset_{flat} refers to the flat earth phase, \emptyset_{topo} is based on the topographic phase or surface elevation, \emptyset_{disp} refers to the displacement phase that represents the displacement of the ground between observations, \emptyset_{atm} is the atmosphere phase, \emptyset_{orbit} is the contribution due to changes in the satellite's orbit and \emptyset_{noise} is the phase noise (Aly et al., 2009; Crosetto et al., 2016; Pepe and Calò, 2017; Höser, 2018). The displacement phase has to be isolated from the other phase components by using various datasets and algorithms (discussed below) to estimate the ground deformation rate between observations (Pepe and Calò., 2017).

- **Phase unwrapping** – restores the correct multiple of 2π to each point of the interferometric phase image to obtain quantitative interpretation (Reigber and Moreira, 1997; Costantini, 1998; Werner et al., 2002).
- **Geocoding** – refers to the projection of the deformation analysis result into a geographic coordinate system (Small and Schubert, 2008). This step is useful as it allows for further analysis and interpretation of the result by integrating with other relevant geocoded datasets and results through the overlay analysis and visualization in a GIS environment (Vallone et al., 2008).

4.3.3. Small Baseline Subset (SBAS)

Though the DInSAR method and the resulting interferogram, derived from two SAR images acquired at different times with the same geometry, is best suited to detect moderate (centimeter)- to large-scale (meter) surface deformation rates resulting from earthquakes and other processes that induce high magnitude displacements, it is not able to discern and quantify slow (millimeter-scale) rates such as slow-moving landslides (Gabriel et al., 1989; Crosetto et al., 2005). Also, the applicability of the method for quantifying landslide velocities is further constrained by the coarse resolution of the DInSAR product and by factors that can affect the interferometric coherence value such as changes in land cover. As a result, some surface features may not be detected because of poor interferometric coherence; hence, their velocities could not be estimated using the DInSAR method (Lanari et al., 2004; Mantovani et al., 2019).

The SBAS technique (Berardino et al., 2002) is an InSAR time series surface deformation inversion method aimed at reducing spatial and temporal decorrelation by selecting image pairs with small spatial orbital separation and temporal baseline for interferogram generation. The technique mitigates some of the limitations posed by the DInSAR method including spatial

decorrelation, phase noise, and the ability to detect subtle (mm-scale) surface displacement rates. This technique was adopted in this study to detect and quantify slow-moving landslides in the study area because of these capabilities. The SBAS method stacks multiple interferograms generated by multi-temporal SAR imagery separated by a threshold-specified spatial and temporal baseline (Berardino et al., 2002; Lanari et al., 2007; Crosetto et al., 2016). The interferograms are multilooked to increase signal-to-noise (SNR) ratios and then unwrapped in space. The interferograms are then stacked together, and pixels that are spatially coherent in most of the interferograms are inverted to estimate displacement rates (Lanari et al., 2007; Zhou et al., 2009; Li et al., 2021).

The SBAS workflow within the SARscape Module of ENVI 5.5 was used for data processing and result (displacement rate) generation. In the first step of the SBAS workflow, a connection network based on the 53 Sentinel-1 images (Table 2) was created (Figure 11) demonstrating the image pairs that will be used for interferogram generation. The connectivity between the interferometric pairs was defined by taking the maximum spatial and temporal baseline threshold values into consideration. In this study, maximum temporal and spatial baseline values of 720 days and 190.9 m were used respectively as cutoff values to create the image pairs required for the subsequent steps. A super reference image (acquired on February 25, 2019) was automatically selected (identified by the yellow dot in Figure 11, and by the dark gray background in Table 2) in this step that was used for coregistering all other images against the geometry of the image in the subsequent steps.

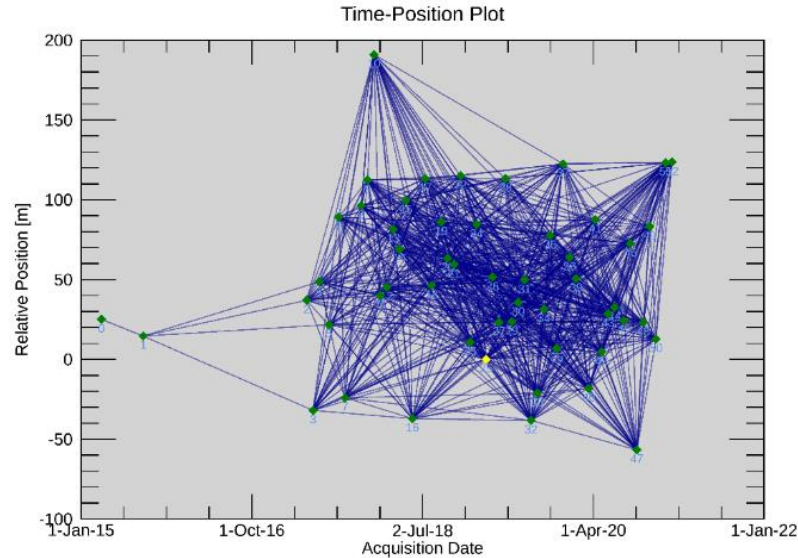


Figure 11: SBAS Interferometric images connection graph, time, and position plot derived from the 53 Sentinel-1 images acquired over the study area. The yellow dot signifies the super reference image, selected by the software, that was used as a reference for the coregistration procedure.

The second step involves the coregistration of the individual images against each other, and with the super reference image. This procedure was followed by the generation of differential interferograms based on the network of pair images established in the first step. Filtering, flattening (flat-earth phase removal) using a 1-arc-second resolution DEM acquired by the Shuttle Radar Topography Mission (SRTM) (Farr and Kobrick, 2000), and phase unwrapping procedures were also executed in this step. Residual non-deformation phase ramps introduced on each of the unwrapped differential interferograms were then estimated and removed in the orbital refinement and re-flattening step. Two inversion steps follow. In the first, the initial estimate of the average displacement rate and residual topography value was calculated. In addition, the interferograms were also unwrapped again to remove any residual topography signal in the final deformation estimate. Displacement time series estimation using the unwrapped interferograms derived in the first inversion step, followed by atmospheric filtering to remove the contribution of atmospheric artifacts on the deformation estimate, was carried out in the second inversion step. The geocoding

of all the processing results by projecting them into a selected cartographic system is performed in the last step. Positive displacement rates signify the movement of the target towards the satellite (uplift), whereas a negative rate implies movement away from the satellite (subsidence) in the repeat observations. A schematic demonstration of the key data processing steps of the SBAS workflow in the SARscape Module of ENVI is shown in Figure 12.

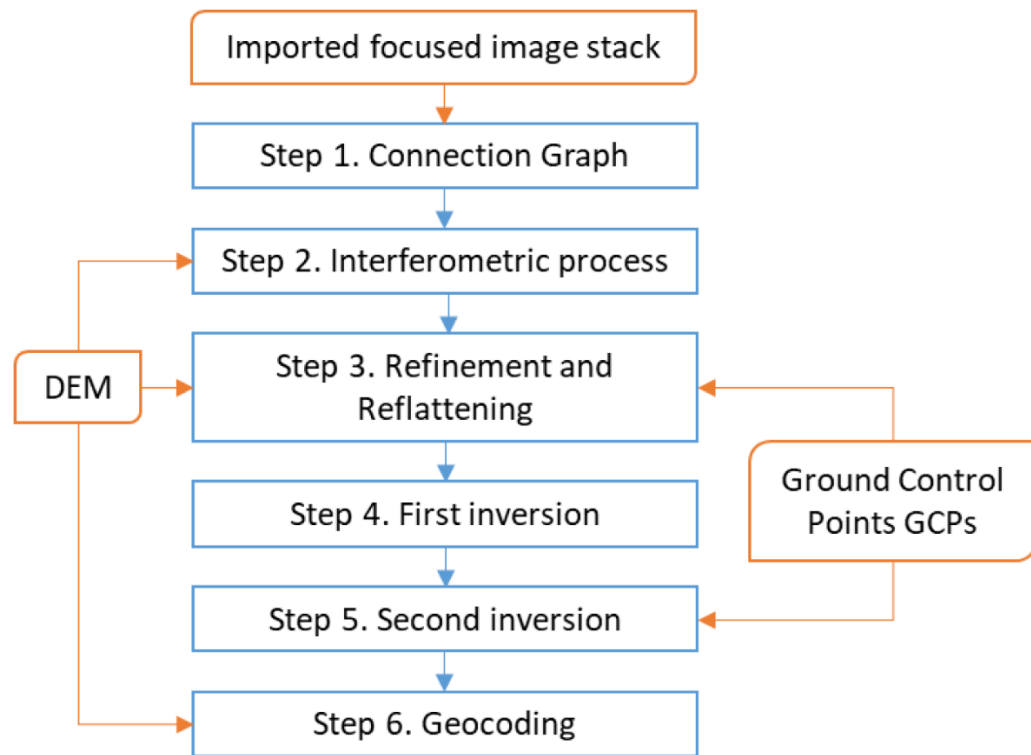


Figure 12: SBAS data processing flowchart (Chen et al., 2021).

4.3.3.1. Calibration and Validation - Global Navigation Satellite System (GNSS) Data

As stated in sub-section 4.3.2, InSAR techniques are prone to many errors from a variety of sources. Although most of the errors are removed through the procedures outlined earlier, residual errors remain that could degrade the quality and accuracy of the deformation estimate. Consequently, calibrating the result with other geodetic techniques improves its accuracy and

validity. Satellite-based geodetic technique has been historically used to track and observe the behavior of mass movements during a landslide as well as other surface deformation processes (Gili et al., 2000; Lazar et al., 2003). This method uses satellite-based GNSS constellation systems to provide positioning, navigation, and timing (PNT) services on a global or regional basis (Langley et al., 2017). As complementary data for calibrating/validating the SBAS result, two GNSS datasets obtained through different geodetic techniques were used. The first set of geodetic data for the study area was acquired from permanent GNSS stations. These stations continuously quantify displacement rates over a wider time scale and can detect subtle (mm-scale) deformation rates. Due to cost and other limitations, the spatial distribution of permanent GNSS is limited in the study area, as well as globally (Carafa et al., 2020). This limitation justifies the need for other options to acquire geodetic datasets in areas where there are no permanent GNSS stations.

Campaign displacement measurements were undertaken in areas where there are no permanent stations to calibrate ongoing active deformation processes driven by slow-moving landslides. Site selection was facilitated by collating the LSM and the SBAS analysis result and identifying potential sites that fall within the high landslide susceptibility zone and exhibit slow to moderate deformation rates. Sites surrounding the Pease Park landslide area that fulfilled these criteria were selected for the campaign investigation.

i. Permanent stations

Permanent GNSS stations, administrated and managed by the National Oceanic and Atmospheric Administration (NOAA) and the National Geodetic Survey (NGS) under the Continuously Operating Reference Stations (CORS) Network, were integrated with the SBAS analysis result to calibrate the deformation rate derived from the SBAS observations. For this

study, displacement rates of the permanent stations named TXAU (Figure 13) obtained from the Nevada Geodetic Laboratory online platform (Blewitt et al., 2018) were used to calibrate and correct the SBAS-based estimates. The TXAU station was selected due to its long period of daily position data (1996–present), and because it is located within the boundaries of the study area. The procedure outlined in Emil et al. (2021) was used to calibrate the SBAS rates using the average vertical displacement rates from the TXAU station. In this method, the average of the SBAS-derived displacement rates of the pixels found within 500 meters radius of the TXAU station were compared with the average long-term displacement rate of the TXAU station. The SBAS rates were then calibrated based on the difference of the values between the average SBAS-derived and GNSS-derived rates.

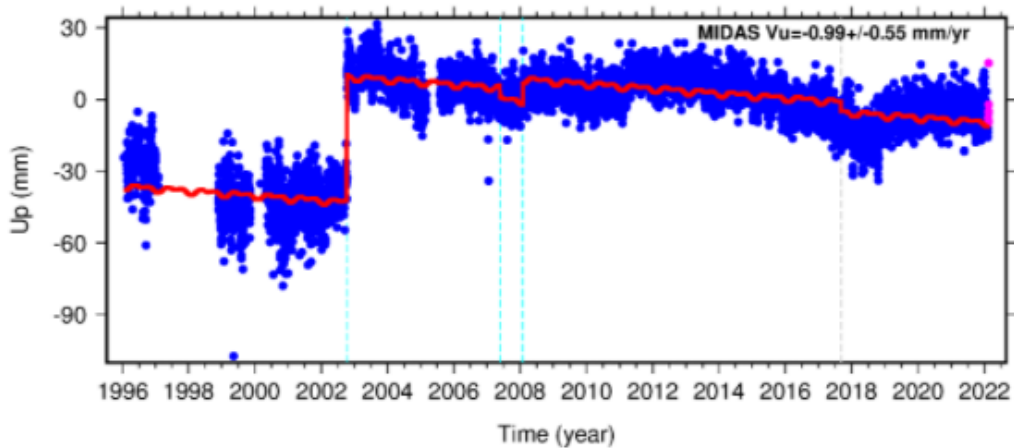


Figure 13: TXAU station daily position data graph from (1996–present).

ii. Campaign measurements

One of the most widely used and reliable geodetic methodologies for tracking mass movement and ground surface deformation rates over time is the multi-temporal Real-Time kinematic (RTK) GNSS survey approach (Rawat et al., 2011). It increases the efficacy to collect larger numbers of high-precision survey position measurements and has been widely used as cross-

validation and calibration for studies using remote sensing techniques (Carlà et al., 2019; Gili et al., 2000). The RTK system provides signal correction through continuous radio communication between a base station and the roving antenna in the field. This system allows to process and view corrected measurements with centimeter to millimeter accuracy in real-time (Lauer, 2021).

For this study, data acquired in two RTK GNSS campaigns further validate the accuracy of the result obtained using the SBAS technique. The focus of the measurements were parts of the study area where active deformation processes have been observed, but permanent GNSS stations were absent. The first measurement campaign was held in August 2021 followed by a second campaign in March 2022. The Emlid Reach RS2 GNSS unit comprising a base station and rover receivers was used for this purpose. Two displacement measurements were made, using the rover receiver, on the steep slopes proximal to the sides of the landslide that occurred along the Shoal Creek Trail in the Pease Park (Figure 14). The reference base station measurement was acquired in a stable zone distant from the unstable slope.



Figure 14: RTK GNSS measurements during the second campaign (March 2022)

4.4. Ancillary Data and Methods

Several data analysis methods were applied on ancillary datasets collected from field surveys to validate the accuracy of the datasets/data descriptions from earlier studies and complement the assessment that is based on remote sensing-based assessment and relevant datasets. These include assessing the lithology and texture of the geologic units as well as the

geometry and features of the slope failure at the Pease Park to help with formulating hypotheses that can explain the mechanisms of the landslide formation process over the study area.

4.4.1. Soil Texture Analysis

Soil texture, defined by its particle size (such as clay, silt, and sand), can play an important role in the slope stability and ground deformation processes (Sidle et al., 1985; Lee et al., 2017). Understanding the complexity and the influence that soil rich in clays may have directly or indirectly while interacting with other factors, allows to observe areas that are more susceptible to the occurrence of slow-moving landslides.

Soil textural analysis method was undertaken in this study to obtain granulometry information of the samples selected from the Pease Park landslide's material and quantify its clay content in the geological formations present. The clay particle size content may significantly contribute to the incidence of a landslide due to the presence of clay layers. Calculating the percentage of clay particles in the samples can be used as a proxy to understand the impact of shrinking and swelling of the clay layers present in the area. The clay content in the geological units could affect the rheology of the units, influencing the degree of swelling and plasticity when exposed to water (Andrade et al., 2011).

A total of 10 soil samples were collected from the Pease Park area for soil textural analysis. The analysis was undertaken following the hydrometer method (using an ASTM 152H-type hydrometer) outlined by Gavlack et al. (2005). In this procedure, the samples were first dried by placing them in a hot air oven at 40°C for 24 hours. After drying, each sample was reduced to small particle size through manual pulverization using a porcelain mortar and pestle. The resulting material was sieved through a 2 mm mesh size (US No. 10 mesh), which is the standard for most soil testing methods (Sikora and Moore, 2014). Thirty grams of the sieved material was then added

to a graduated cylinder of 1000 ml to determine the amount of sand, silt, and clay present in the sample. The particle size segregation was estimated by measuring how fast the material settled out of a water-based solution based on the three main size classes of soil particles: sand (50–2000 μm), silt (2.0–50 μm), and clay ($< 2.0 \mu\text{m}$). The results were plotted in the Soil Textural Triangle to collect relative proportions of sand, silt, and clay in the samples.

4.4.2. Unmanned Aircraft Systems (UAS)

As a result of the large spatial scale of the landslide event that occurred in the Pease Park coupled with the inaccessibility of the area, it was not possible to observe the entire area to get detailed information on the scarp, crown, and other geometric information to accurately understand the formation mechanism of the event. A close investigation of the area was made possible through the generation of a 3D model of the landslide geometry by using the SfM algorithm applied on a high-resolution image acquired by the DJI Spark UAS. The SfM procedure was facilitated using the cloud based DroneDeploy software. In addition to providing a closer look at the geometry of the slope failure at Pease Park, the 3D model also helped for having a closer look at the fractures and other geological features that directly or indirectly contributed to the occurrence of the event. Also, it assisted in visually corresponding the lithology of the scarp and the geological material observed at the foot of the hill during field visits.

CHAPTER FIVE

RESULTS AND DISCUSSION

5.1. Overview

This chapter provides a detailed and comprehensive perspective of the results produced using the datasets, methods, and tools (software) that were outlined in detail in chapter four. Also, in-depth discussions on the interpretation of the results and the relationship between the individual results derived from different approaches, and their overall collective influence on landslide susceptibility of Austin City and its surroundings is provided.

5.2. Analyses of Factors Controlling Landslide Susceptibility

The six factors that were considered in this study as controlling factors for the incidence of landslides over the study area (sub-section 4.2), namely slope gradient, land use, geology, geological structures, drainage network, and precipitation were integrated to determine the susceptibility of the different parts of the study area for landslide hazards.

The slope gradient was considered to play an important role in this study since most landslide occurrences across the globe are related to the slope angle. The slope gradient map of the study area (Figure 15) shows that the angle values range from less than 5° to 87° . The slope gradient was classified into four groups ($<5^{\circ}$), $(5-14^{\circ})$, $(14-37^{\circ})$, and $(37-87^{\circ})$). This is done based on a combination of the natural distribution and classification of the data (natural break's classification scheme) as well as considering classification schemes in previous studies in the study area and elsewhere (Wachal and Hudak, 2000; Canavesi et al., 2020; Sifa et al., 2020). For example, Pachauri and Pant (1992) noted that there is a strong correlation between the frequency of occurrences of landslides and steeper slope angles ($> 35^{\circ}$). In this study, areas with slope angle less than 5° are classified as the flattest terrain with low susceptibility to landslide incidence,

whereas terrains with slope angles higher than 37° are considered highly vulnerable to slope instability. This vulnerability is because slope steepening leads to an increase in the shear force and a decline in the normal force (Figure 1) that may give rise to a slope failure (Bizimana and Sönmez, 2015; Johnson et al., 2017). Most areas within the study area lie on a gentle slope (less than 5°). Steep slope angles ($> 37^\circ$) are noted in sites close to drainage networks, in areas with abrupt elevation changes probably resulting from differential erosion (such as in terraces), and in the western hilly terrains of the study area (Figure 15). The Pease Park area, where the recent landslides occurred, and the surrounding areas (shown in a red-outlined box in Figure 15) lie on a moderate to steep slope terrain ($> 14^\circ$).

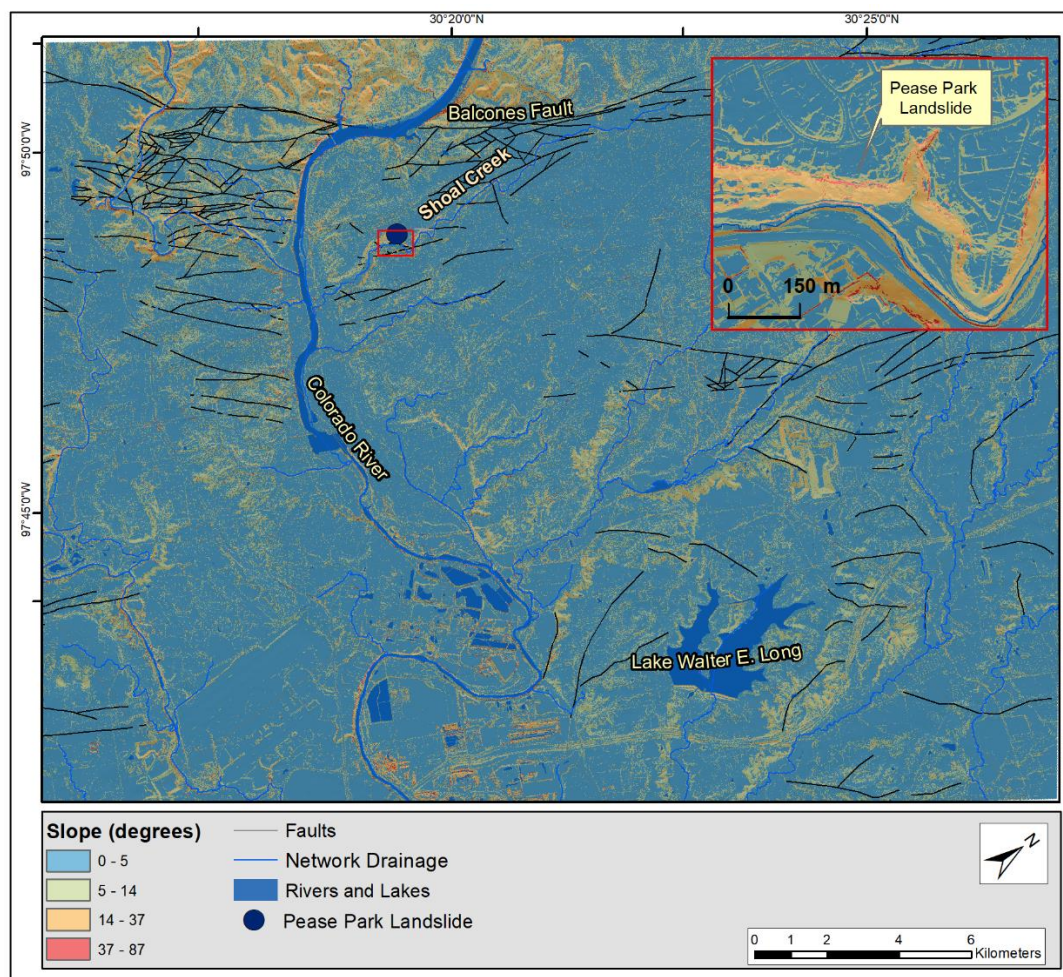


Figure 15: Slope analysis map of the study area derived using high-resolution LiDAR DEM.

The second controlling factor considered in this study was the land cover type (Figure 16). The study area was classified into four major groups based on the type of ground cover present at the time of data acquisition (land cover). The NLCD land classification data was re-classified from the original sixteen classes into four new classes taking the dominant vegetation types and land cover conditions of the study area into consideration. The four classes are forest/woodland, shrubland/grassland, cropland, and urban/bare soil classes (Figure 16). The purpose of the re-classification procedure was to accomplish two major considerations outlined by Wachal and Hudack's (2000) analysis. First, areas with scattered vegetation are more susceptible to the occurrence of a landslide than areas with a higher density of vegetation. It has been proven that vegetation root networks help support slope stability through mechanical reinforcement of the slope, and the removal of water from the soil and geologic units through evapotranspiration (Wu, 1984; Moresi et al., 2020). Therefore, areas with sparse vegetation tend to be more susceptible to landslides than areas with dense vegetation. Additionally, areas that are intensely urbanized and have agricultural development are more susceptible as a result of the alteration of the natural properties and conditions of the soil (Giordan et al., 2017). Second, urbanization processes and agriculture activities can cause slope disturbances as well as aggravate slope weathering and erosion processes thereby creating a conducive setting for slope failure incidence (Hung et al., 2016). Croplands and urban/bare soil cover make up about 63% of the study area. Most of the northern, western, and southwestern parts of the study area fall into the urban/bare soil category, followed by the spots of croplands distributed mostly in the northeast and southeast regions (Figure 16). Areas with moderate to dense vegetation, considered less likely settings for landslide occurrence, are sparsely distributed across the study area including the northwestern, eastern, and southern parts of the study area (Figure 16).

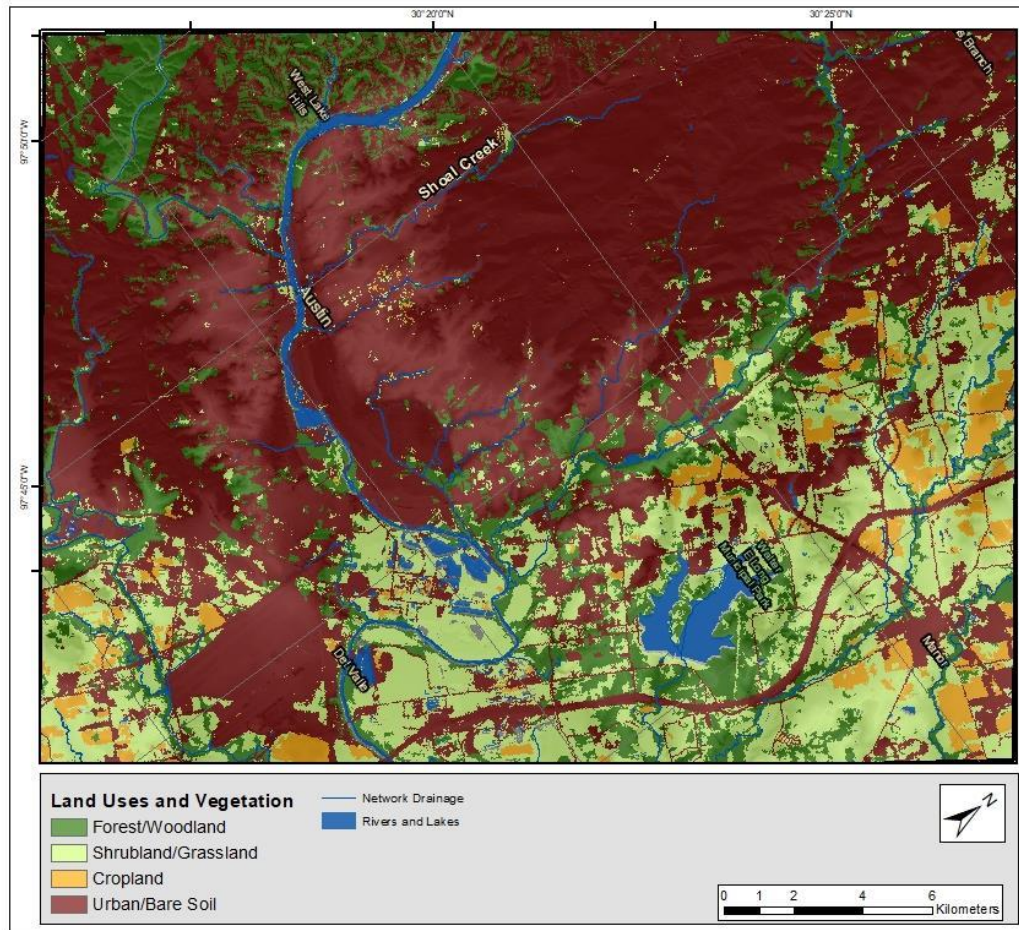


Figure 16: The spatial distribution of the different land cover types of the study area.

The third controlling factor considered was the geology of the study area. The fifteen lithological units prevalent in the study area (Table 3, Figure 17) were classified into four different classes, namely strong, slightly strong, moderate, and weak, based on their composition, comparative cohesive strength, and stability as measured by the degree of weathering and impact by BFZ and other tectonic structures in the study area (Table 3). The detailed lithological descriptions of the units in the study area provided by the USGS (<https://mrdata.usgs.gov/>) and other previous studies (e.g., Young, 1977) were assessed to categorize the units into four classes. In addition, the classification approach outlined by Wachal and Hudak (2000) was also considered. In that study (Wachal and Hudak, 2000), the geology of Travis County was classified into four

classes in which limestone units were considered the most stable lithology of the area, followed by the marls, shales, and finally, the most unstable units that comprise unconsolidated materials or weathered and fractured rocks. In this study, the unconsolidated material, which includes the Quaternary alluvium, terrace deposits, and high gravel deposits, the fractured and weathered limestones of the Buda and Eagle Ford formations, the Del Rio Formation and the fractured limestone from Georgetown Formation, and the mudstone-claystone from the Neylandville and Marlbrook formations were classified as “weak” material. These units are dominantly observed in the area surrounding the BFZ (including the Shoal Creek area), along the lower sections of the Colorado River, and pockets spread across the study area with significant distribution noted in the western and southwestern sections of the study area (Figure 17). The “moderate” class constitutes the alkalic basalt and pyroclastic rocks altered to clay from the Cretaceous igneous rocks, the siltstone-mudstone and incidental limestone from the Navarro and Taylor Group, and the mudstone-claystone from the Ozan Formation. The geologic units in the southern and eastern sections of the study area fall under this category (Figure 17). The Austin Chalk and Navarro Group, comprising marlstone, chalk, and limestone, were classified as “slightly strong”. This class is notably observed in northern and northeastern parts while small patches of the class are noted in the southern part of the study area (Figure 17). Units categorized under the “strong” classification include the limestone units from the Edwards Limestone, the Fredericksburg Group, the Glen Rose Limestone, and the Pecan Gap Chalk. These units are mainly distributed in the western section of the study area and on the west side of Lake Walter E. Long (Figure 17).

Table 3: Lithological Classification of the study area (modified from Wachal and Hudak (2000)).

Geology	Description	Classification
Alluvium	flood plain deposits: sand, silt, clay, and gravel	Weak
Terrace Deposits	sand, silt, clay, and variable size gravel	Weak
High gravel deposits	high gravel deposits	Weak
Igneous rocks	pyroclastic altered to clay	Moderate
Pecan Gap	chalk	Strong
Ozan	marl and clay	Moderate
Navarro/Taylor	marl and clay	Moderate
Austin	chalk and marl	Strong
Eagle Ford/Buda	shale and limestone	Slightly strong
Del Rio / Georgetown	clay and marl	Weak
Fredericksburg	limestone and marl	Strong
Edwards	limestone, dolomite, and chert	Strong
Glen Rose	limestone, dolomite, and marl	Strong
Neylandville /Marlbrook	shale and marl	Slightly strong
Navarro/Marlbrook	limestone and marl	Slightly strong

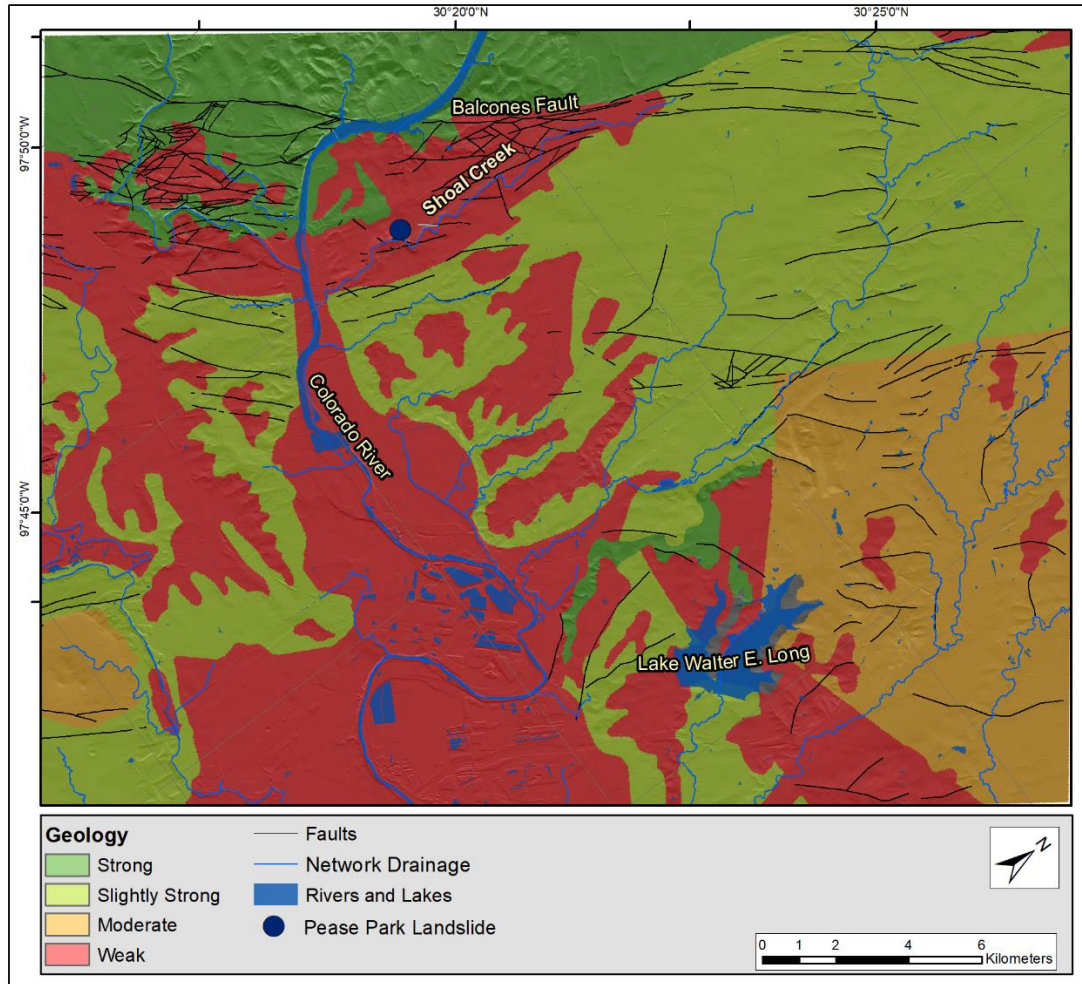


Figure 17: Classification of the geological units in the study area based on the perceived cohesive strengths and stability of the units.

For assessing the influence of faults and fractures on landslide susceptibility, a series of buffered zones were created based on the proximity of the zones (areas) to the nearest tectonic feature. Four zones with 500-meter incremental Euclidean distances from the features were created (Figure 18). Areas located within 500 meters from the nearest faults and fractures were considered the most susceptible material with a higher impact on landslide generation. The following zone was considered with distances between 500 and 1000 meters as the second most susceptible areas, whereas areas between 1000 and 1500 meters and greater than 1500 meters were considered as moderate and least susceptible areas, respectively.

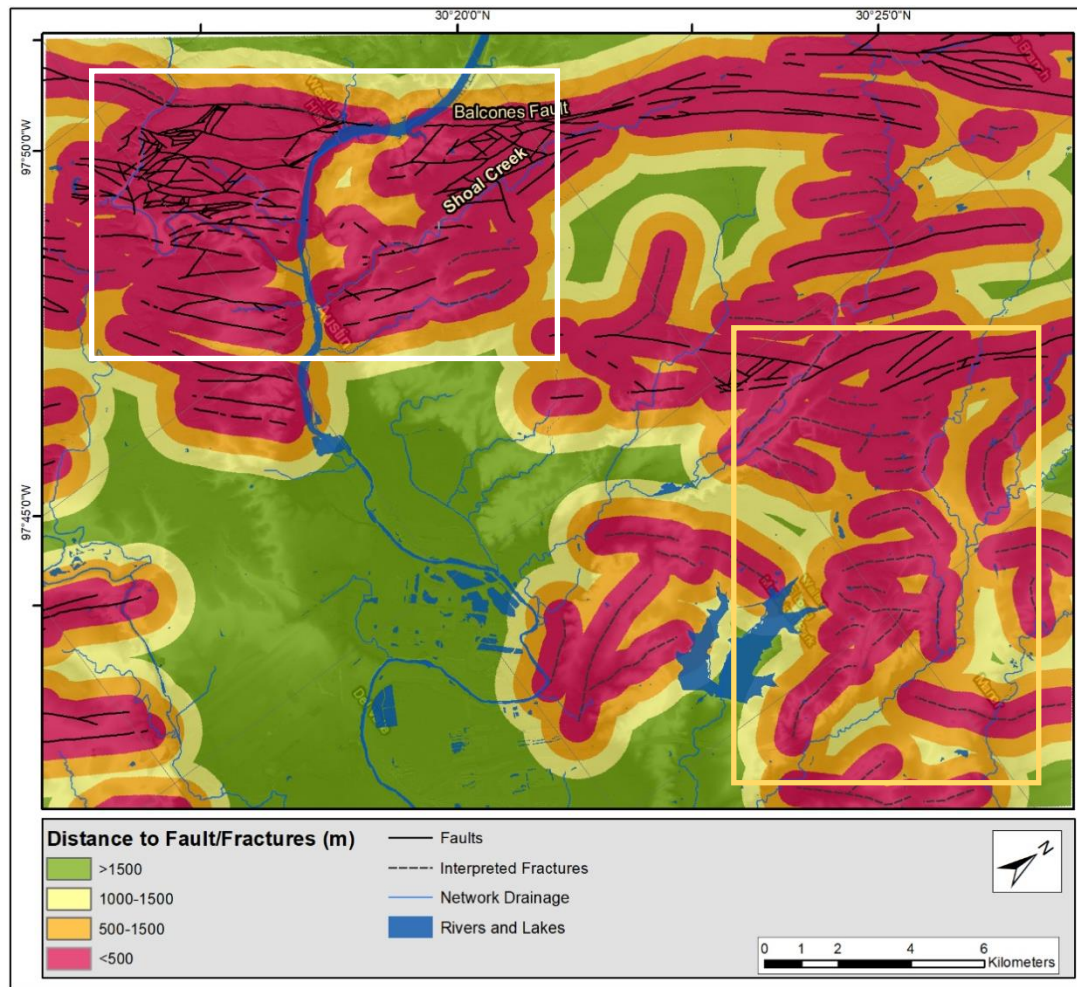


Figure 18: Fault and fracture buffer zones indicating the susceptibility of areas to landslide based on their proximity to the structures. Areas located within 500-m radius of the features are considered highly susceptible to landslide hazards. The white-outlined box demonstrates the dense network of tectonic features noted close to the BFZ.

The area surrounding the Balcones fault (Figure 18) includes a series of geological structures and features such as normal faults, grabens, and horsts (shown in a white-outlined box in Figure 18). This highly fractured and faulted zone is spatially concentrated in the western portion of the study area (Figure 18) where some of the geological units closer to the fault and fracture system distinctly exhibit higher levels of weathering and fracturing making the materials lose their cohesive strength (Ferrill and Morris, 2008). Some of the lithological units are those categorized under the Del Rio and Buda Formations. Additional fractures were inferred using techniques

applied on Sentinel-1 SAR imagery as discussed earlier (sub-section 4.2.1). The delineated structures (shown in dashed black and red lines in Figures 18 and 19, respectively) were mostly concentrated in the eastern and northeastern quadrants of the study area (shown in yellow-outlined boxes in Figures 18 and 19). Buffer zones demonstrating the proximity of areas to these structures, as was done to the existing tectonic features (reported in the literature), were also created for the newly mapped structures.

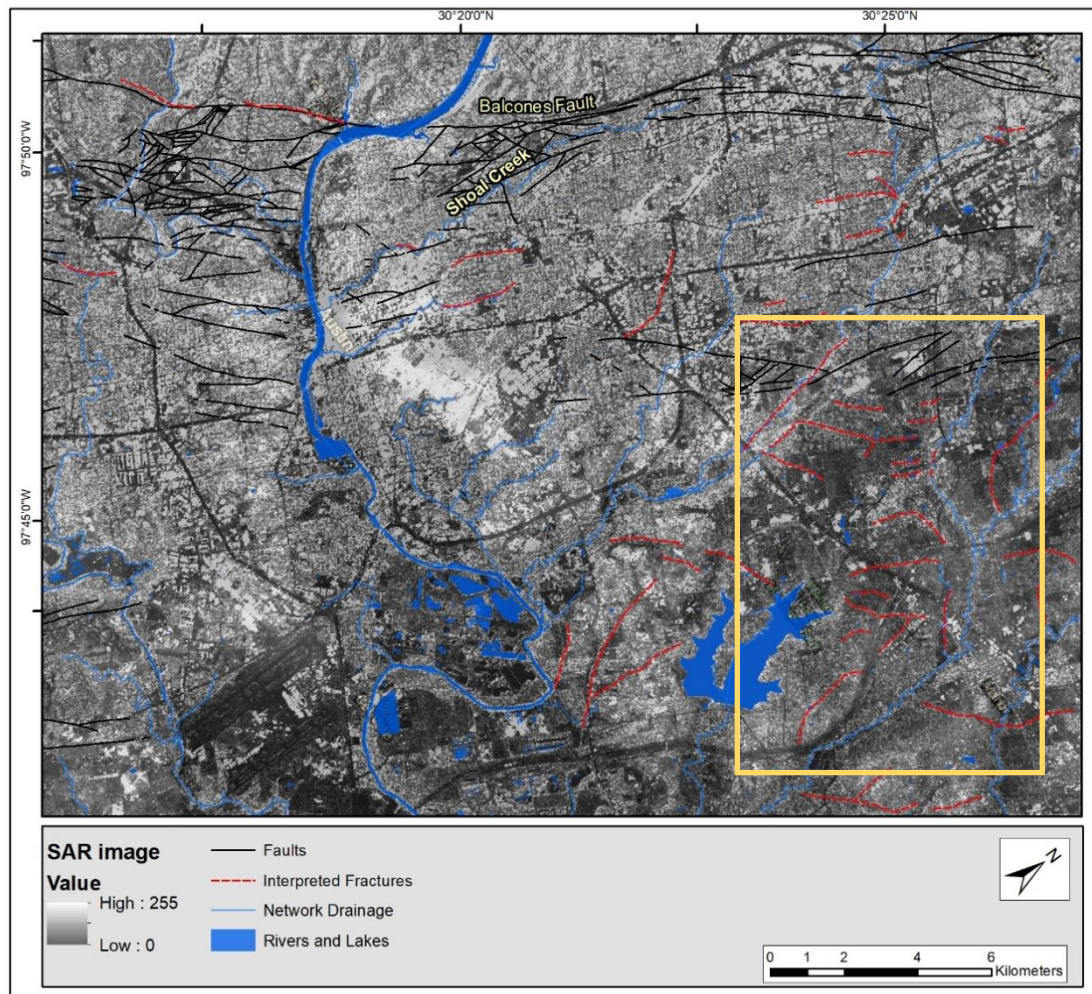


Figure 19: Inferred tectonic features of the study area based on Sentinel-1 SAR image and DEM data.

The last two factors considered in this study with respect to their influence on the incidence of slope failures were the distance to drainage channels and the amount of precipitation received.

To investigate the role of distance from drainage networks on landslide susceptibility, four buffer zones were created by setting incremental distances from each one of the drainage networks in the study area (Figure 20): distances from 0 to 200 meters, 200 to 800 meters, 800 to 1,400 meters, and greater than 1400 meters. As stated earlier, the susceptibility of areas to landslide hazards is inversely proportional to their location with respect to the networks. That is, buffers with a greater distance from the drainage networks have the lowest impact on landslide triggering factors, and buffers closer to the networks were attributed to areas with a higher level of vulnerability. Several studies noted that areas located within a distance of 200 meters are susceptible to landslide hazards, though aquifer properties control the rate and extent of the water flow within the units, given that other conditions that induce the hazard are met (e.g., Moharrami et al., 2020). The notion behind setting the cutoff value in this study was that the dense network of faults and fractures across the study area could create favorable conditions for the water to propagate through units found proximal to the networks (Hauwert and Vickers, 1994) and may induce landslide in the nearby areas through processes and interactions outlined in sub-section 4.2.1.

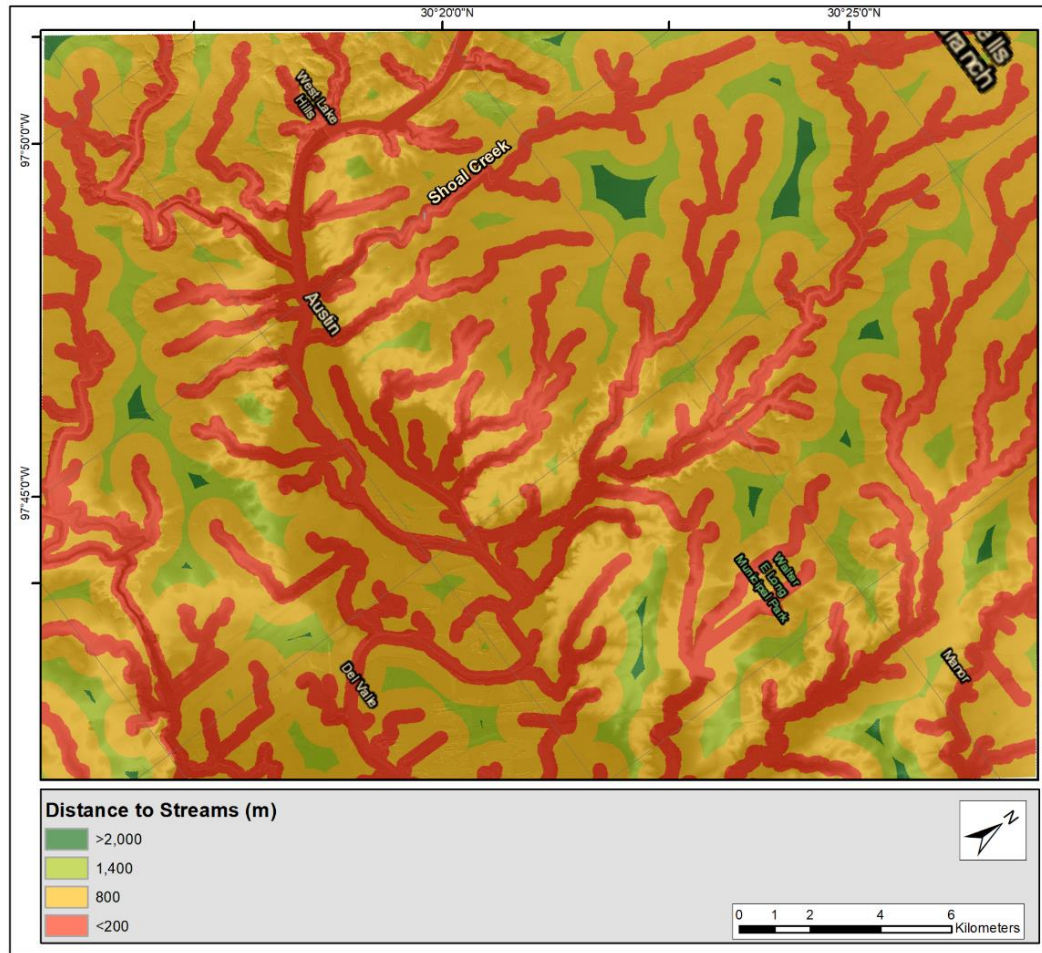


Figure 20: Drainage buffer zones indicating the susceptibility of areas to landslide based on their proximity to drainage networks.

The mean annual precipitation values over the study area were calculated based on the PRISM gridded data (1981–2019). A mean annual precipitation value raster surface was generated using the Inverse Distance Weighted (IDW) interpolation method. The precipitation data, as the other controlling factors analyzed previously, was classified into four classes based on the natural break classification scheme: 852–863 mm/yr; 863–870 mm/yr; 870–877 mm/yr; and greater than 877 mm/yr (Figure 21). Overall, the precipitation data across the study area does not show a significant change between each of the four grids. The difference in the mean annual precipitation value between the lower limits of the class with lower the higher precipitation annual value has a mere 25 mm/year (Figure 21). This difference shows that if other conditions that may induce

landslide susceptibility are met, almost all areas within the study area could be prone to the hazard considering the precipitation variable. It is also possible that though the mean annual rainfall over a given area might be slightly lower than the surrounding, isolated episodes of intense precipitation may drive slope failure events as was the case in the Pease Park area.

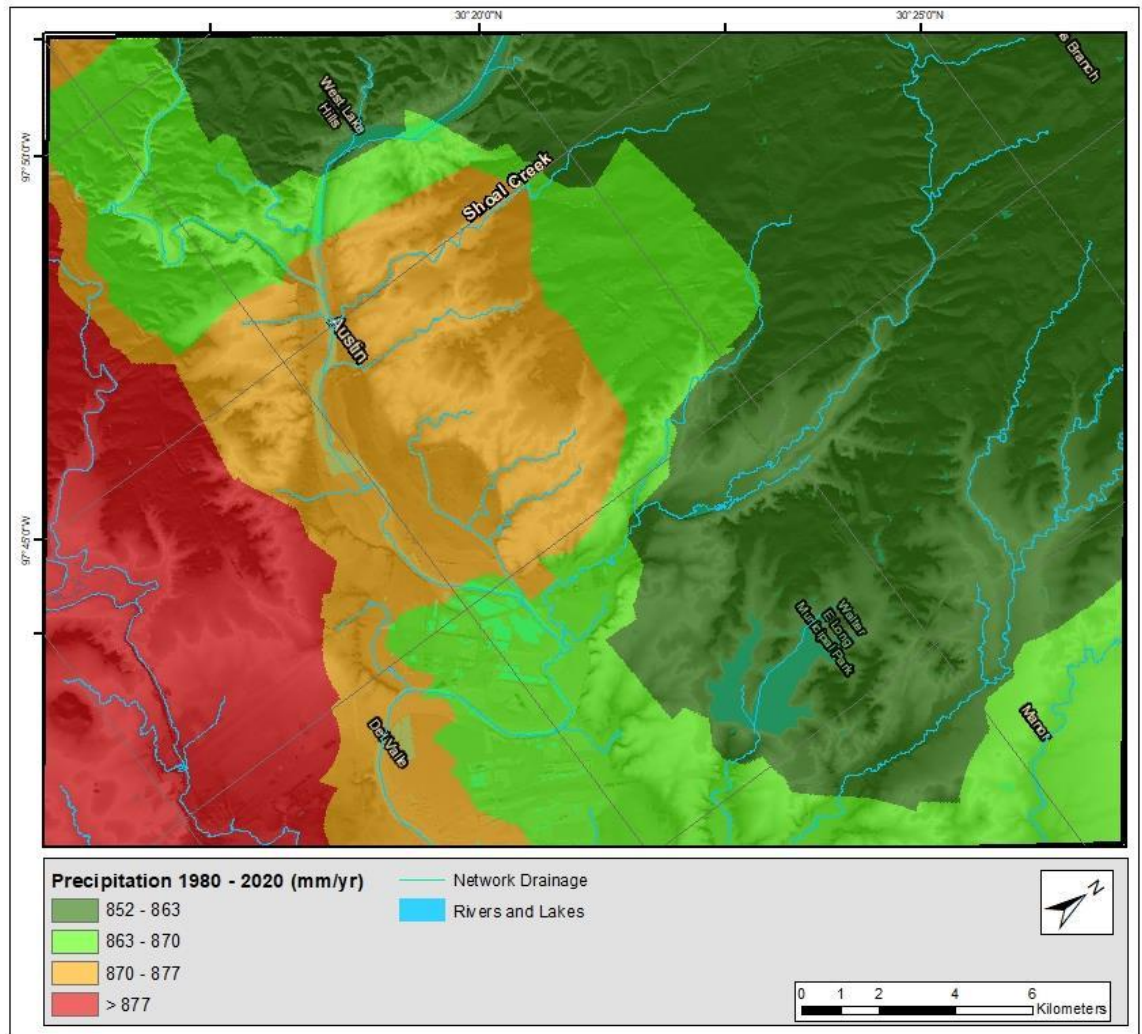


Figure 21: Classification of the study area based on the amount of mean precipitation received (1981–2019)

5.3. Landslide Susceptibility Map

The defined classes of each of the controlling factors described above were given a rating value, ranging from 1 to 4, and weight values signifying the level of importance of the controlling factor in initiating a landslide hazard were given following the approach outlined in sub-section 4.2.2. The assigned rating system per class in each of the controlling factors and the assigned weight of each of the controlling factors are shown in Table 4. The weight assignment took local conditions and the perceived influences of the different factors in instigating the landslide event in the Pease Park (Shoal Creek) area into consideration. As described above, part of the Shoal Creek trail (Pease Park) where two recent landslides were recorded (May 2018 and May 2019) lies on a moderate to steep slope ($> 14^\circ$) that receives a moderate amount of annual rainfall. Also, the site is located proximal to a drainage network, is heavily dissected by a network of tectonic features, and is underlain by weak geologic units. An empirical assessment of the relative influences of the factors was made and weights were assigned as a result. In addition, assessments during field investigations, as well as approaches outlined in earlier studies (Sarkar et al., 1995; Wachal and Hudak, 2000; Loucks, 2018) to identify the significance of the different factors were used to assign weights for the controlling factors. The slope gradient was assigned the highest weight (25%), while the other five factors were applied equal weights (15%), owing to the change in slope angle being the most critical controlling factor that may initiate a slope failure. With increasing slope angles, the shear stress on the slope material will also increase (Yalcin, 2007), which may lead to slope failure when coupled with the other controlling factors and processes that result in decreased shear strength of the materials. The LSI values were then calculated by combining the assigned weights and rating values using the WLC approach (sub-section 4.2.2).

Table 4: Weight and rating assigned to each of the controlling factors. The slope gradient was assigned a higher weight (1.5 times higher than the weight assigned to the other factors).

Controlling Factors	Weight	Rating
Slope (degrees)	25%	
0–5		1
5–14		2
14–37		3
37–86		4
Land Cover	15%	
Forest/Woodland		1
Shrubland/Grassland		2
Cropland		3
Urban/Bare Soil		4
Geology	15%	
Limestone		1
Shale		2
Marl		3
Unconsolidated		4
Distance to Fault/fractures (m)	15%	
>1500		1
1000–1500		2
500–1500		3
<500		4
Precipitation (mm/yr)	15%	
852–863		1
863–870		2
870–877		3
→ 877		4
Distance to Drainage (m)	15%	
>1400		1
800–1400		2
200–800		3
<200		4

The resulting LSI values were classified using the natural break classification scheme into four susceptibility groups to generate the LSM of the study area (Figure 22). The categories were: (i) null to low susceptibility, (ii) medium susceptibility, (iii) medium-high susceptibility, and (iv) high susceptibility.

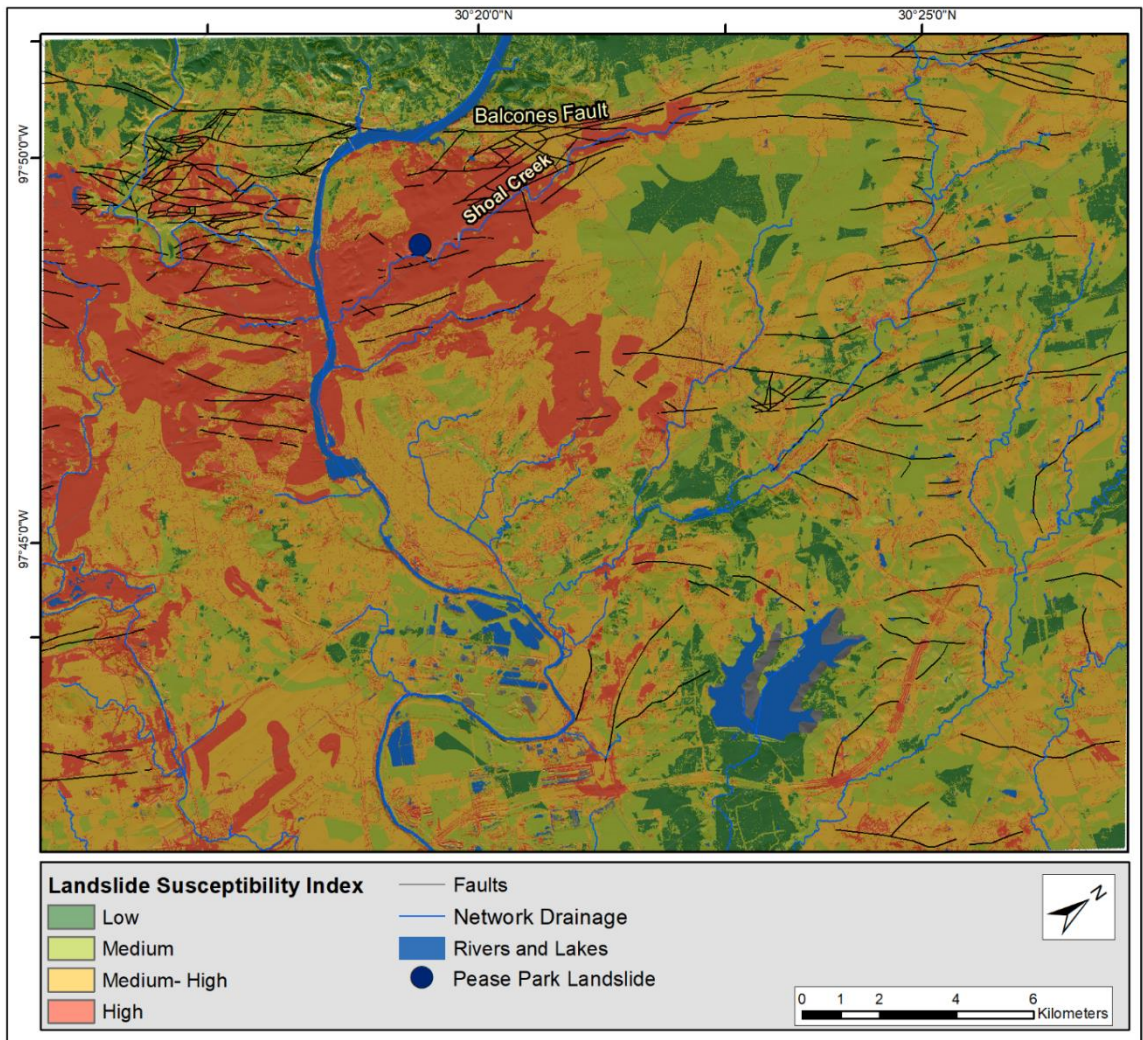


Figure 22: Landslide susceptibility map of Austin City and surroundings.

A simple statistical analysis of the percentage distribution of the different landslide susceptibility categories over the study area (Table 5) shows that 16.8% of the study area falls under the high susceptibility category, medium-high susceptibility is 31%, while the percentages of parts of study area falling under the medium and low categories stand at 33.1% and 19.1, respectively (Table 5).

Table 5: Analysis indicating the area and percentage coverage of the landslide susceptibility categories.

Susceptibility Index	Coverage (km²)	Percentage (%)
Low	112.7	19.1
Medium	195.2	33.1
Medium-High	183.1.5	31
High	98.9	16.8

Areas categorized under the medium susceptibility class have lithology dominated by the Marl and Limestone from the Navarro Group, Navarro and Taylor; Neylandville and Marlbrook Marls, and the Ozan Formations (Figures 6, 7, and 22; Table 3). Parts of the study area falling under the low susceptibility category correspond spatially with the geological units that exhibit cohesion and strength and that were earlier classified as ‘strong’ geological units (Figures 17 and 22; Table 3). That is, the most stable areas in the study area, in part or fully, are overlain by the Glen Rose Formation, Fredericksburg Group, Pekan Gap Chalk, Austin Chalk, and the Edwards Limestone units (Figures 6 and 22). Even areas lying on steep slopes but dominated by these units exhibit low susceptibility to landslide hazards (Figures 6, 17, and 22). But it would be inaccurate to assume that there is a linear relationship between geology (composition, strength, stability) and landslide susceptibility since the other controlling factors also influence the outcome of the suitability analysis over a given area. The medium and low susceptible classes are spatially distributed across the study area with high prevalence noted in the north, northwestern, and southeastern parts of the study area (Figure 22). Areas classified under the medium-high susceptibility category are underlain by weak to moderate units such as terrace deposits, gravel deposits, and patches of the Glen Rose Formation and the Fredericksburg Group (Figures 6, 17, and 22). This medium-high susceptibility category is concentrated in the central, southern, and southeastern parts of the study area. The highest susceptibility class represents areas with the greatest vulnerability to the impacts of landslide hazards. Areas falling under this category, dominantly observed in the western and southwestern parts, lie on moderate to steep slopes ($> 37^\circ$) with the land cover types that are predominantly urban/developed or bare soil with a low vegetation index. The principal lithological units that make up this category include the fractured and weathered limestones from the Eagle Ford, Georgetown, and Buda Formations, clay and other units of the Del Rio Formation, and patches of gravel and terrace deposits. The sites in this category

lie proximal to geological structures and drainage networks with maximum distances of 500 m and 200 m, respectively. In addition, these areas get a mean annual precipitation value of more than 870 mm. The Pease Park area falls under the high susceptible category (Figure 22).

It is hypothesized in this study that the landslide processes in the study area are slow-moving types (discussed in sub-section 5.4), but intense rainfall or flooding episodes amplify the probability of occurrence of landslides in the high susceptible areas that are dissected by a network of tectonic features. The successive slope failure events that transpired at the Pease Park along the Shoal Creek following the reported prolonged intense rainfall (Shoal Creek Conservancy, 2020) attest to this hypothesis. It is suggested in this study that the mechanism of the slope failure in the area was initiated through the percolation of rainwater through the network of faults and fractures in the overlying Buda Formation. The subsequent interaction with the swelling, plastic Del Rio clay at depth created conducive setting for the landslide events to occur. The hydration of the montmorillonite and kaolinite minerals that exist in the Del Rio formation (Garner and Young, 1976) leads to changes in the molecular structure of the mineral. This changes are because when water gets absorbed within the layers of the clay, the mineral structure expands causing swelling, especially in montmorillonite clays, and increases the shear stress on the slope material (Yalcin, 2007; Earle, 2015; Soto et al., 2017; Iqbal et al., 2018). As a result, shear strength is reduced and the clay layer acts as a slip surface causing slope failure (Yalcin, 2007; Chandler, 2020). It is postulated in this study that the event that led to the formation of the Shoal Creek landslide events occurred following the processes outlined above through years of gradual displacement of the material (discussed below), but the displacement rates and the subsequent failures were enhanced by the intense precipitation episodes. Besides the two relatively massive episodes of slope failure in the area, it has been reported that similar precipitation events have induced landslides in the past (Shoal Creek Conservancy, 2020).

The 3D model generated using the SfM algorithm applied on the data acquired by the UAS (Figure 23) supports the above-stated assessment on the mechanisms of the slope failure at the Pease Park. A closer investigation reveals a rotational type of slide (Figure 23) whose occurrence was likely facilitated by the percolation of (rain)water through the preferential pathways (fractures – shown by red lines) in the weathered and fractured Buda Formation and the ensuing interaction with the underlying Del Rio Formation (Figure 23).



Figure 23: A 3D model of the Pease Park (Shoal Creek) landslide created using data acquired by the UAS. The fractured and weathered Buda limestone is shown overlying the Del Rio clay. The fracture paths within the limestone layer through which water from the surface percolates into the subsurface and interact with the Del Rio clay layer are shown in red. The inset on the right side is a zoomed-in view showing the contact between the limestone from the Buda Formation and a softer greyish stratum from the Del Rio Formation.

To validate the composition of the material whose interaction with water presumably induced the landslide at the Pease Park site, soil samples were collected from the failure material and a complementary soil textural analysis was undertaken. The results of the analysis show a high percentage of clay- and silt-sized-particles (Figure 24).

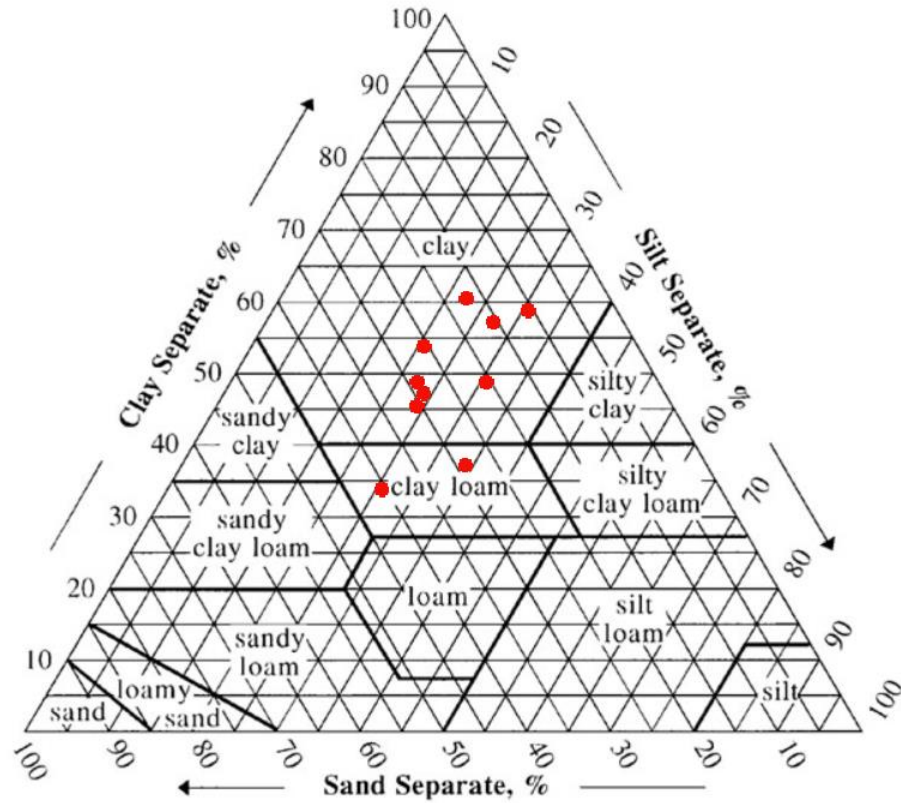


Figure 24: Soil texture triangle depicting the textural composition of the samples collected from the Pease Park (Shoal Creek). The plot was constructed using the U.S. Department of Agriculture’s Natural Resources Conservation Service (NRCS) platform (<https://www.nrcs.usda.gov/>)

5.4. SBAS

Because the LSM shows the probability of occurrence of all types of landslides, it is important to supplement the analysis with the integration of other datasets and methods to identify slow-moving slides and quantify their displacement rates, which would be crucial for early-warning and disaster mitigation purposes. The evaluation of displacement rates was carried out by using the SBAS analysis technique applied to SAR data sets. The SBAS analysis technique was applied on fifty-three Interferometric Wide Sentinel-1 SAR datasets acquired from March 2015 to January 2021 (Figure 8). The result was calibrated using the deformation rate (-0.89 ± 0.54 mm/yr (1996–2021)) retrieved from the (TXAU) permanent GNSS station (shown in red fill star with black outline in Figure 25) The ground deformation velocity values across the study area (Figure

25a) range from -9.35 to 10.31 mm/yr (positive displacement rates signify uplift while negative rates represent the movement of the target away from the satellite (subsidence) - subsection 4.3.3). The majority parts of the study area exhibit a stable to uplift (> -1 mm yr) deformation pattern (Figure 25a). Small clusters of high rates of subsidence values (< -3.07 mm/yr) (shown in dark orange colors in Figure 25a) were noted in the north and northeastern parts of the study area. Representative sites (randomly) were selected for field investigation (shown in boxes highlighted in red (sites A, B and C) in Figure 25a) to determine the possible causes of the high rates of subsidence observed and to assess whether the processes were related to landslides activities. As a result, areas under construction (or recently completed construction) where new soil materials were added to the sites and the landscape changed dramatically between 2015 and 2021. The time-lapse (2016 and 2021) Google Earth images of the sites (Figure 25b) depicted the land surface changes that occurred in these areas during the investigated interval. These surface modifications generated strong subsidence signals in the SBAS analysis. It is possible that accelerated compaction of the newly added soil material resulted in the observed high rates of subsidence over these areas. Hence, it was concluded that the processes and rates observed in these areas were not related to landslide activities. This displacement rates indicates that not all displacement signals shown in Figure 25a should be interpreted as areas experiencing slope failure. Hence, high subsidence rates (< -3.07 mm/yr) were excluded from the slope failure analysis.

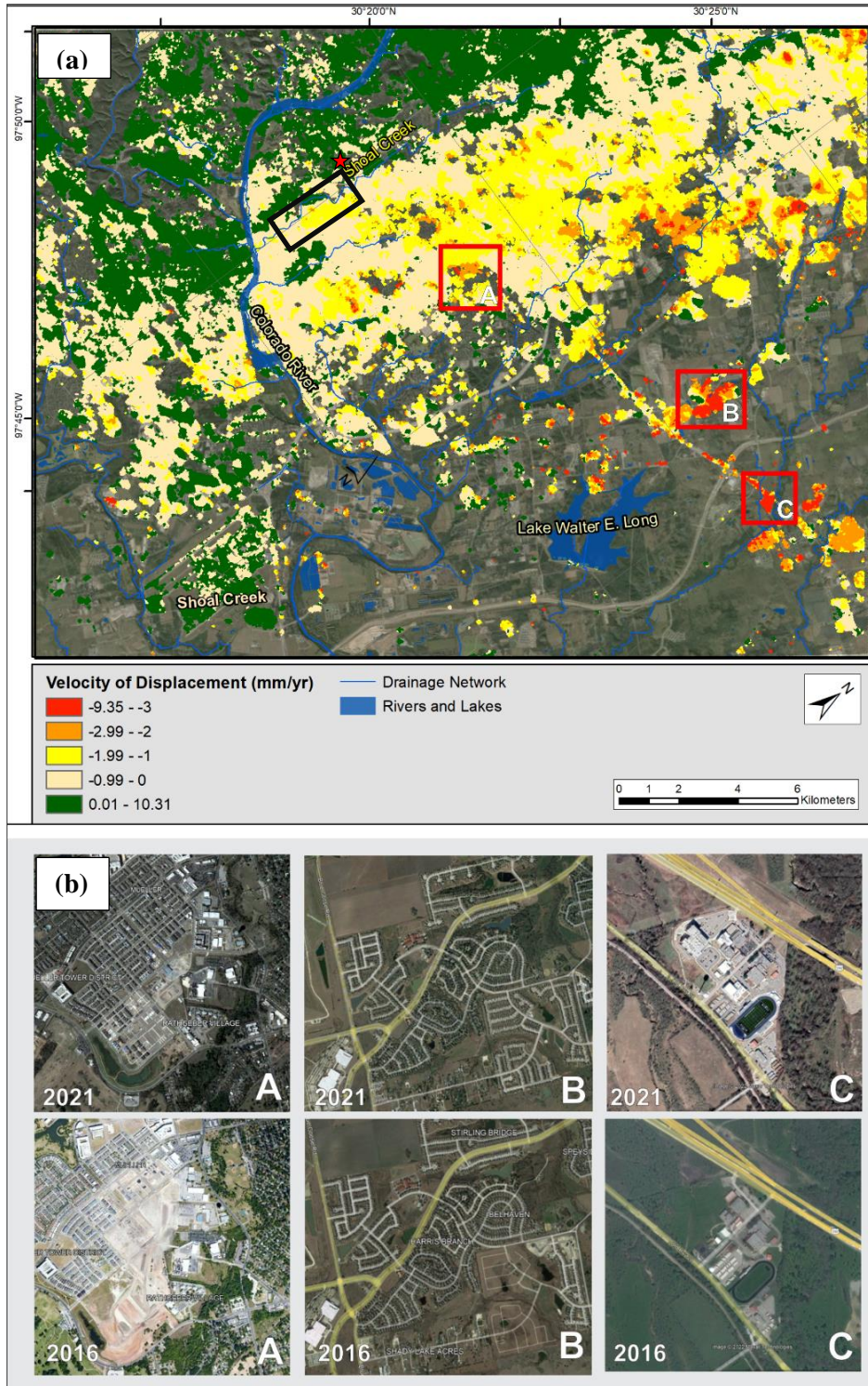


Figure 25: (a) Surface deformation analysis of the study area derived using the SBAS technique applied on SAR datasets. The three sites that were selected for field assessment to determine the causes of the high subsidence rates are shown in red-outlined boxes. The Pease Park area where recent landslides have occurred is shown in a black-outlined box; (b) Time-lapse (2015–2021) Google Earth images of the investigated sites (A, B, and C) were visited. The red star polygon with a black outline indicates the location of the GNSS station (TXAU) that was used for calibration purposes.

In this study, small to moderate subsidence rates (-1 to -3.06 mm/yr) were taken as a measure of (identifying) slow-moving slides. Hungr et al. (2014) suggested that slow-moving slides, especially rotational slides, may initially exhibit a slow rate of movement but this can change into a rapid movement in the occurrence of triggering events such as earthquakes or heavy rainfall. But it should be noted again that not all observed low rates of displacement were attributed to landslide processes. A comparison of the LSM (Figure 22) and the SBAS deformation analysis result (Figure 25a) reveals a pattern of spatial correlation between the two results along the medium-high and high susceptibility areas (Figure 22), and the moderate subsidence rates (Figure 25a) in the north and northwestern parts of the study area. For example, the LSM map indicated high levels of landslide susceptibility for the Pease Park area. The deformation analysis of the area (shown in the black-outlined box in Figure 25a) showed low to moderate subsidence rates (-1 to -3.06 mm/yr) that indicate an active slow-moving landslide activity. Field investigations corroborated this assessment that the ground surface in the area is in a continuous motion. For instance, tilted trees or trees with bent stems were observed in parts of the Pease Park area surrounding the previous slope failure (Figure 26).



Figure 26: Areas surrounding the Pease Park landslide show signs of active displacement activity (tilted trees on the left, and bent stem on the right) that supports the slow rate of displacement estimated using the SBAS technique (Figure 25).

In addition to the visual observations, the analysis results of the multi-temporal GNSS RTK measurements collected from the area (Pease Park) showed an ongoing displacement activity. Though some sites where initial measurements (August 2021) were taken were inaccessible due to floods during the second visit (March 2022), GNSS measurements were made at a single site and corresponded with the earlier result. The result indicated a higher displacement rate (up to – 17 mm/month) between the two intervals (Table 6). Though the result showed a relatively higher displacement/subsidence rate than that was reported by the SBAS analysis, that may be due to atmospheric conditions during the second measurement, or a high displacement rate induced by intense precipitation episodes in the days before the field visit, it nevertheless showed the presence of an ongoing activity around the creek area as demonstrated by the SBAS result.

Table 6: Displacement rate (given in mm/month) calculated using multi-temporal (7-month interval) GNSS RTK measurements.

Positioning Point	Longitude (decimal degrees)	Latitude (decimal degrees)	Elevation (m)	Elevation change (mm/month)
DATE 1: 08-11-2021				-17
Point_A	-97.75100997	30.29192035	126.307	
DATE 2: 03-11-2022				
Point_A	-97.75101006	30.29192036	126.190	

Though intense rainfall was considered in this study as the main trigger that enhances the displacement rates of slow-moving slides and results in slope failures, a thorough assessment of other potential factors that directly or indirectly contribute to this process should be made in future studies. Particularly, the influence of anthropogenic activities on inducing slope failures should be investigated. The effects of land cover change, largely caused by anthropogenic activities, were partly investigated in this study, but a more in-depth assessment of this and other anthropogenic-related factors using datasets with inherent uniform and improved spatial resolution (without resampling) would be beneficial. This factor is important, as the city of Austin and its surroundings are experiencing rapid development without a detailed assessment of anthropogenic changes on landslide processes. As a result, the landslide hazards repercussion on communities and resources could not be avoided.

CHAPTER SIX

CONCLUSION

During the past decade, the City of Austin and its surroundings have undergone massive development in terms of urbanization and population growth. The high population growth rate has led to population expansion into areas that are susceptible to natural hazards. Landslide is one of the hazards that parts of the city experienced in recent years. In addition to the natural factors and processes that induce landslides, the intense anthropogenic activity that accompanied urbanization also impacts this phenomenon, increasing the community's susceptibility to the hazard.

In this research, LSM was generated using various relevant datasets integrated and analyzed in a GIS environment. The LSM was accomplished by evaluating six controlling factors including slope gradient, land cover, geologic units, geologic structures, distance to the drainage network, and precipitation. The controlling factors were classified, rated, and assigned weights based on their role in initiating landslides in the study. The resulting LSM map indicated that the sections of the western and southwestern parts of the study area, comprising about 16.8% of the study area, are highly susceptible to a landslide hazard. These high landslide susceptible areas receive moderate amounts of precipitation (mean annual precipitation > 870 mm), lie on moderate to steep slopes (> 37°) that are proximal to geological structures and drainage networks, and have low to moderate levels of vegetation cover. The fractured and weathered limestones from the Eagle Ford, Georgetown, and Buda Formations, clay from the Del Rio Formation, and patches of gravel and terrace deposits underline these areas. The cumulative effects of percolation of water through the network of faults and fractures in the Buda Formation and interaction with the swelling montmorillonite- and kaolinite-bearing Del Rio Clay at depth and the resulting changes in shear strength of the slope material were credited in this study as the main mechanism of formation of

landslide in the study area. The proposed hypothesis was tested through the analysis of the UAV data-derived 3D model of the landslide that occurred in the Pease Park along the Shoal Creek trail. The composition of the material from the slip surface was also analyzed to validate the clay lithology of the material (Del Rio Formation) that induced the slope failure.

SBAS deformation analysis using fifty-three Sentinel-1 images was undertaken to identify active slow-moving slides and quantify their displacement rates that would be crucial for early-warning and disaster mitigation purposes. The result was calibrated and validated using results from a permanent station and multi-temporal RTK-GNSS measurements. The slow-moving slides in the study area exhibited a deformation rate ranging from -1 to -3.06 mm/yr. A comparison of the spatial distribution of the slow-moving slides derived using the SBAS technique with the LSM result showed a pattern of spatial correlation between the medium-high and high susceptibility areas and the slow-moving slides in the north and northwestern parts of the study area.

The methods and techniques demonstrated in this research can be used by the community and policymakers as input to investigate similar problems in other areas that are at risk from the threats of landslide hazards to develop landslide early-warning systems.

REFERENCES

- Abedini, M., and Tulabi, S. (2018). Assessing LNRf, FR, and AHP models in landslide susceptibility mapping index: a comparative study of Nojian watershed in Lorestan province, Iran. *Environmental Earth Sciences*, 77(11), 1–13.
- Abella, E. A. C., and Van Westen, C. J. (2008). Qualitative landslide susceptibility assessment by multicriteria analysis: a case study from San Antonio del Sur, Guantánamo, Cuba. *Geomorphology*, 94(3–4), 453–466.
- Adkins, W. S., and Lozo, F. E. (1951). *Stratigraphy of the Woodbine and Eagle Ford, Waco area, Texas*.
- Ahmed, B. (2015). Landslide susceptibility mapping using multi-criteria evaluation techniques in Chittagong Metropolitan Area, Bangladesh. *Landslides*, 12(6), 1077–1095.
- Aleotti, P., and Chowdhury, R. (1999). Landslide hazard assessment: summary review and new perspectives. *Bulletin of Engineering Geology and the Environment*, 58(1), 21–44.
- Aly, M. H., Zebker, H. A., Giardino, J. R., and Klein, A. G. (2009). Permanent Scatterer investigation of land subsidence in Greater Cairo, Egypt. *Geophysical Journal International*, 178(3), 1238–1245.
- Andrade, F. A., Al-Qureshi, H. A., and Hotza, D. (2011). Measuring the plasticity of clays: a review. *Applied Clay Science*, 51(1–2), 1–7.
- Arabameri, A., Rezaei, K., Cerdà, A., Conoscenti, C., and Kalantari, Z. (2019). A comparison of statistical methods and multi-criteria decision making to map flood hazard susceptibility in Northern Iran. *Science of the Total Environment*, 660, 443–458.
- Ayalew, L., Yamagishi, H., and Ugawa, N. (2004). Landslide susceptibility mapping using GIS-based weighted linear combination, the case in Tsugawa area of Agano River, Niigata Prefecture, Japan. *Landslides*, 1(1), 73–81.
- Baker, V. R. (1975). Flood hazards along the Balcones escarpment in central Texas; alternative approaches to their recognition, mapping, and management. *Virtual Landscapes of Texas*. <https://repositories.lib.utexas.edu/bitstream/handle/2152/77739/txu-oclc-1967634.pdf>
- Bamler, R., and Hartl, P. (1998). Synthetic aperture radar interferometry. *Inverse Problems*, 14(4), R1–R54. <https://doi.org/10.1088/0266-5611/14/4/001>
- Barker, R. A., Bush, P. W., and Baker, E. T. (1994). *Geologic history and hydrogeologic setting of the Edwards-Trinity aquifer system, west-central Texas* (Issue 94). US Department of the Interior, US Geological Survey.
- Barnes, V.E., Hartmann, Barbara, and Scranton, D. F. (1992). *Geologic map of Texas, 1:500,000*. https://ngmdb.usgs.gov/Prodesc/proddesc_68390.htm
- Barnes, V.E., Co., S. O., Humble Oil and Refining Co., Mobile Oil Co., Proctor, C.V., Brown, T. E., McGowen, J. H., Waechter, N. B., Eargle, D. H., Baker, E. T., Peckman, R. C., and Bluntzer, R. L. (1981). *Geologic atlas of Texas, Austin sheet*. University of Texas at Austin, Bureau of Economic Geology. https://ngmdb.usgs.gov/Prodesc/proddesc_16440.htm
- Berardino, P., Fornaro, G., Lanari, R., and Sansosti, E. (2002). A new algorithm for surface deformation monitoring based on small baseline differential SAR interferograms. *IEEE*

Transactions on Geoscience and Remote Sensing, 40(11), 2375–2383.

- Bixler, R. P., Yang, E., Richter, S. M., and Coudert, M. (2021). Boundary crossing for urban community resilience: A social vulnerability and multi-hazard approach in Austin, Texas, USA. *International Journal of Disaster Risk Reduction*, 66, 102613.
- Bizimana, H., and Sönmez, O. (2015). Landslide occurrences in the hilly areas of Rwanda, their causes and protection measures. *Disaster Science and Engineering*, 1(1), 1–7.
- Blanco-Sánchez, P., Mallorquí, J. J., Duque, S., and Monells, D. (2008). The Coherent Pixels Technique (CPT): An Advanced DInSAR Technique for Nonlinear Deformation Monitoring. *Earth Sciences and Mathematics*, 1167–1193. https://doi.org/10.1007/978-3-7643-8907-9_10
- Blewitt, G., Hammond, W., and Kreemer, C. (2018). Harnessing the GPS Data Explosion for Interdisciplinary Science. *Eos*, 99. <https://doi.org/10.1029/2018EO104623>
- Blumberg, D. G. (1998). Remote sensing of desert dune forms by polarimetric synthetic aperture radar (SAR). *Remote Sensing of Environment*, 65(2), 204–216.
- Brune, G., Duffin Geologists, G. L., Nemir, C. E., Beecherl, L. A., Mccleskey, G. W., Roney, G. E., Bo, L. A. ", Pilgrim, ", Bankston, W. O, Welch, L., Mcdonald, F., Biggart, L. B. M., and Stover, J. D. (1983). *Texas Department of Water Resources Report 276 Occurrence, Availability, And Quality of Ground Water in Travis County, Texas Texas Department of Water Resources*.
- Bullard, F. J. (1953). Polymorphinidae of the Cretaceous (Cenomanian) Del Rio shale. *Journal of Paleontology*, 338–346.
- Butler, D. R. (2021). *Texas Almanac: Physical Regions of Texas*. <https://www.texasalmanac.com/articles/physical-regions>
- Canavesi, V., Segoni, S., Rosi, A., Ting, X., Nery, T., Catani, F., and Casagli, N. (2020). Different approaches to use morphometric attributes in landslide susceptibility mapping based on meso-scale spatial units: A case study in Rio de Janeiro (Brazil). *Remote Sensing*, 12(11), 1826.
- Carafa, M. M. C., Galvani, A., Di Naccio, D., Kastelic, V., Di Lorenzo, C., Miccolis, S., Sepe, V., Pietrantonio, G., Gizzi, C., and Massucci, A. (2020). Partitioning the ongoing extension of the central Apennines (Italy): Fault slip rates and bulk deformation rates from geodetic and stress data. *Journal of Geophysical Research: Solid Earth*, 125(7), e2019JB018956.
- Carlà, T., Tofani, V., Lombardi, L., Raspini, F., Bianchini, S., Bertolo, D., Thuegaz, P., and Casagli, N. (2019). Combination of GNSS, satellite InSAR, and GBInSAR remote sensing monitoring to improve the understanding of a large landslide in high alpine environment. *Geomorphology*, 335, 62–75. <https://doi.org/10.1016/J.GEOMORPH.2019.03.014>
- Castro, J., Asta, M. P., Galve, J. P., and Azañón, J. M. (2020). Formation of clay-rich layers at the slip surface of slope instabilities: the role of groundwater. *Water*, 12(9), 2639.
- Çellek, S. (2020). Effect of the slope angle and its classification on landslide. *Natural Hazards and Earth System Sciences Discussions*, 1–23.
- Chalkias, C., Ferentinou, M., and Polykretis, C. (2014). GIS-based landslide susceptibility mapping on the Peloponnese Peninsula, Greece. *Geosciences*, 4(3), 176–190.
- Chandler, R. J. (2020). Processes leading to landslides in clay slopes: a review. *Hillslope*

Processes, 343–360.

- Chen, X., Achilli, V., Fabris, M., Menin, A., Monego, M., Tessari, G., and Floris, M. (2021). Combining Sentinel-1 Interferometry and Ground-Based Geomatics Techniques for Monitoring Buildings Affected by Mass Movements. *Remote Sensing*, 13(3), 452.
- Clark, A. K., Golab, J. A., and Morris, R. R. (2020). *Geologic framework and hydrostratigraphy of the Edwards and Trinity aquifers within northern Bexar and Comal Counties, Texas*. US Geological Survey.
- Corominas, J., van Westen, C., Frattini, P., Cascini, L., Malet, J.-P., Fotopoulou, S., Catani, F., Van Den Eeckhaut, M., Mavrouli, O., and Agliardi, F. (2014). Recommendations for the quantitative analysis of landslide risk. *Bulletin of Engineering Geology and the Environment*, 73(2), 209–263.
- Costantini, M. (1998). A novel phase unwrapping method based on network programming. *IEEE Transactions on Geoscience and Remote Sensing*, 36(3), 813–821.
- Crosetto, M., Crippa, B., and Biescas, E. (2005). Early detection and in-depth analysis of deformation phenomena by radar interferometry. *Engineering Geology*, 79(1–2), 81–91. <https://doi.org/10.1016/J.ENGGEOL.2004.10.016>
- Crosetto, M., Monserrat, O., Cuevas-González, M., Devanthéry, N., and Crippa, B. (2016). Persistent Scatterer Interferometry: A review. *ISPRS Journal of Photogrammetry and Remote Sensing*, 115, 78–89. <https://doi.org/https://doi.org/10.1016/j.isprsjprs.2015.10.011>
- Crosta, G. B., Imposimato, S., and Roddeman, D. G. (2003). Numerical modelling of large landslides stability and runout. *Natural Hazards and Earth System Sciences*, 3(6), 523–538.
- Cutrona, L. J. (1990). Synthetic aperture radar. *Radar Handbook*, 2, 2333–2346.
- Dai, F. C., Lee, C. F., Li, J., and Xu, Z. W. (2001). Assessment of landslide susceptibility on the natural terrain of Lantau Island, Hong Kong. *Cases and Solutions Environmental Geology*, 40(3).
- Daly, C. (2006). Guidelines for assessing the suitability of spatial climate data sets. *International Journal of Climatology: A Journal of the Royal Meteorological Society*, 26(6), 707–721.
- Earle, S. (2015). *15.1 Factors That Control Slope Stability*. <https://opentextbc.ca/geology/chapter/15-1-factors-that-control-slope-stability/>
- El Jazouli, A., Barakat, A., and Khellouk, R. (2019). GIS-multicriteria evaluation using AHP for landslide susceptibility mapping in Oum Er Rbia high basin (Morocco). *Geoenvironmental Disasters*, 6(1), 3. <https://doi.org/10.1186/s40677-019-0119-7>
- Emil, M. K., Sultan, M., Alakhras, K., Sataer, G., Gozi, S., Al-Marri, M., and Gebremichael, E. (2021). Countrywide Monitoring of Ground Deformation Using InSAR Time Series: A Case Study from Qatar. *Remote Sensing*, 13(4), 702.
- Farr, T. G., and Kobrick, M. (2000). *Shuttle Radar Topography Mission Produces a Wealth of Data PAGES 583,585*. <http://www.jpl.nasa.gov/srtm/>.
- Feizizadeh, B., and Blaschke, T. (2011). Landslide risk assessment based on GIS multi-criteria evaluation: a case study in Bostan-Abad County, Iran. *Journal of Earth Science and Engineering*, 1(1), 66–77.
- Ferrill, D. A., and Morris, A. P. (2008). Fault zone deformation controlled by carbonate

- mechanical stratigraphy, Balcones fault system, Texas. *AAPG Bulletin*, 92(3), 359–380.
- Ferring, C. R. (2007). *The Geology of Texas*. www.thomsonedu.com/earthscience.
- Firomsa, M., and Abay, A. (2019). Landslide assessment and susceptibility zonation in Ebantu district of Oromia region, western Ethiopia. *Bulletin of Engineering Geology and the Environment*, 78(6), 4229–4239.
- Fitch, J. P. (2012). *Synthetic aperture radar*. Springer Science and Business Media.
- Flores-Anderson, A. I., Herndon, K. E., Thapa, R. B., and Cherrington, E. (2019). *The SAR handbook: Comprehensive methodologies for forest monitoring and biomass estimation*. <https://earthdata.nasa.gov/learn/backgrounders/what-is-sar>
- Gabriel, A. K., Goldstein, R. M., and Zebker, H. A. (1989). Mapping small elevation changes over large areas: Differential radar interferometry. *Journal of Geophysical Research: Solid Earth*, 94(B7), 9183–9191. <https://doi.org/10.1029/JB094IB07P09183>
- Garello, R. (2010). Signal and image processing applications in radar ocean observations. *10th International Conference on Information Science, Signal Processing and Their Applications (ISSPA 2010)*, 810–818. <https://doi.org/10.1109/ISSPA.2010.5605405>
- Garner, L. E., Young, K. P., Rodda, P. U., Dawe, G. L., and Rogers, M. A. (1976). Environmental geology of the Austin area: an aid to urban planning. *Walter Geology Library*.
- Gavlack, R., Horneck, D., and Miller, R. (2005). *Plant, soil and water reference methods for the Western Region. Western Regional Extension Publication (WREP) 125, WERA-103 Technical Committee*.
- Gebremichael, E. G. (2018). *Assessing Land Deformation and Sea Encroachment in the Nile Delta: A Radar Interferometric and Modeling Approach*.
- Gili, J. A., Corominas, J., and Rius, J. (2000). Using Global Positioning System techniques in landslide monitoring. *Engineering Geology*, 55(3), 167–192. [https://doi.org/10.1016/S0013-7952\(99\)00127-1](https://doi.org/10.1016/S0013-7952(99)00127-1)
- Giordan, D., Cignetti, M., Baldo, M., and Godone, D. (2017). Relationship between man-made environment and slope stability: the case of 2014 rainfall events in the terraced landscape of the Liguria region (northwestern Italy). *Geomatics, Natural Hazards and Risk*, 8(2), 1833–1852.
- Glade, T., Anderson, M. G., and Crozier, M. J. (2006). *Landslide hazard and risk*. John Wiley and Sons.
- Gökçeoglu, C., and Aksoy, H. (1996). Landslide susceptibility mapping of the slopes in the residual soils of the Mengen region (Turkey) by deterministic stability analyses and image processing techniques. *Engineering Geology*, 44(1–4), 147–161.
- Guzzetti, F., Carrara, A., Cardinali, M., and Reichenbach, P. (1999). Landslide hazard evaluation: a review of current techniques and their application in a multi-scale study, Central Italy. *Geomorphology*, 31, 181–216.
- Guzzetti, F., Mondini, A. C., Cardinali, M., Fiorucci, F., Santangelo, M., and Chang, K.-T. (2012). Landslide inventory maps: New tools for an old problem. *Earth-Science Reviews*, 112(1–2), 42–66.

- Hammons A. (2018). *Several Central Austin homes near edge of new cliff after Shoal Creek landslide* / WOAI. NEWS4SA. <https://news4sanantonio.com/news/local/four-central-austin-homes-near-edge-of-new-cliff-after-shoal-creek-landslide>
- Hanssen, R. F. (2001). *Radar interferometry: data interpretation and error analysis* (Vol. 2). Springer Science and Business Media.
- Hauwert, N., and Vickers, S. (1994). *Barton Springs/Edwards aquifer hydrogeology and groundwater quality*.
- He, Q., Shahabi, H., Shirzadi, A., Li, S., Chen, W., Wang, N., Chai, H., Bian, H., Ma, J., and Chen, Y. (2019). Landslide spatial modelling using novel bivariate statistical based Naïve Bayes, RBF Classifier, and RBF Network machine learning algorithms. *Science of the Total Environment*, 663, 1–15.
- Helz, R. L. (2021a). *InSAR—Satellite-Based Technique Captures Overall Deformation “Picture.”* Volcano Hazards Program. <https://www.usgs.gov/programs/VHP/insar-satellite-based-technique-captures-overall-deformation-picture>
- Helz, R. L. (2021b). *InSAR—Satellite-based technique captures overall deformation “picture”* | U.S. Geological Survey. <https://www.usgs.gov/programs/VHP/insar-satellite-based-technique-captures-overall-deformation-picture>
- Highland, L. M., and Bobrowsky, P. (2008). The landslide Handbook - A guide to understanding landslides. *US Geological Survey Circular*, 1325. <https://doi.org/10.3133/cir1325>
- Hill, R. T. (1977). *Geologic Atlas of Texas; Del Rio Sheet. Scale 1: 250000*.
- Hill, Robert T, and Vaughan, T. W. (1902). Description of the Austin quadrangle. *US Geol. Survey Geol. Atlas, Austin Folio*, 76, 8.
- Hilley, G. E., Bürgmann, R., Ferretti, A., Novali, F., and Rocca, F. (2004). Dynamics of slow-moving landslides from permanent scatterer analysis. *Science*, 304(5679), 1952–1955.
- Höser, T. (2018). *Analysing the capabilities and limitations of InSAR using Sentinel-1 data for landslide detection and monitoring*. Master’s Thesis, Department of Geography, University of Bonn, Bonn, Germany.
- Housh, T. B. (2007). *Bedrock Geology of Round Rock and Surrounding Areas, Williamson and Travis Counties, Texas*.
- Hung, L. Q., Van, N. T. H., Duc, D. M., Ha, L. T. C., Van Son, P., Khanh, N. H., and Binh, L. T. (2016). Landslide susceptibility mapping by combining the analytical hierarchy process and weighted linear combination methods: a case study in the upper Lo River catchment (Vietnam). *Landslides*, 13(5), 1285–1301.
- Hungr, O., Leroueil, S., and Picarelli, L. (2014). The Varnes classification of landslide types, an update. *Landslides*, 11(2), 167–194.
- Hylland, M. D., Black, B. D., and Lowe, M. (1997). Geologic hazards of the Wasatch Front, Utah. *Brigham Young University Geology Studies*, 42(2), 299–324.
- Intrieri, E., Carlà, T., and Gigli, G. (2019). Forecasting the time of failure of landslides at slope-scale: A literature review. *Earth-Science Reviews*, 193, 333–349.
- Iqbal, J., Dai, F., Hong, M., Tu, X., and Xie, Q. (2018). Failure mechanism and stability analysis of an active landslide in the xiangjiaba reservoir area, southwest china. *Journal of Earth*

Science, 29(3), 646–661.

- Iverson, R. M., and Major, J. O. N. J. (1987). Rainfall, ground-water flow, and seasonal movement at Minor Creek landslide, northwestern California: Physical interpretation of empirical relations. *GSA Bulletin*, 99(4), 579–594. [https://doi.org/10.1130/0016-7606\(1987\)99<579:RGFASM>2.0.CO;2](https://doi.org/10.1130/0016-7606(1987)99<579:RGFASM>2.0.CO;2)
- Johnson, Chris; Affolter Matthew D.; Inkenbrandt, P. ; M. C. (2017). *An Introduction to Geology*. Salt Lake Community College. <https://opengeology.org/textbook/>
- Kanungo, D. P., Arora, M. K., Sarkar, S., and Gupta, R. P. (2006). A comparative study of conventional, ANN black box, fuzzy and combined neural and fuzzy weighting procedures for landslide susceptibility zonation in Darjeeling Himalayas. *Engineering Geology*, 85(3–4), 347–366.
- Kirschbaum, D. B., and Fukuoka, H. (2012). Remote sensing and modeling of landslides: Detection, monitoring and risk evaluation. In *Environmental Earth Sciences* (Vol. 66, Issue 6). <https://doi.org/10.1007/s12665-012-1543-0>
- Klimeš, J., and Rios Escobar, V. (2010). A landslide susceptibility assessment in urban areas based on existing data: an example from the Iguaná Valley, Medellín City, Colombia. *Natural Hazards and Earth System Sciences*, 10(10), 2067–2079.
- Kritikos, T. R. H., and Davies, T. R. H. (2011). GIS-based multi-criteria decision analysis for landslide susceptibility mapping at northern Evia, Greece. *Zeitschrift Der Deutschen Gesellschaft Für Geowissenschaften*, 421–434.
- Lacroix, P., Araujo, G., Hollingsworth, J., and Taïpe, E. (2019). Self-Entrainment Motion of a Slow-Moving Landslide Inferred From Landsat-8 Time Series. *Journal of Geophysical Research: Earth Surface*, 124(5), 1201–1216.
- Lacroix, P., Bièvre, G., Pathier, E., Kniess, U., and Jongmans, D. (2018). Use of Sentinel-2 images for the detection of precursory motions before landslide failures. *Remote Sensing of Environment*, 215, 507–516.
- Lacroix, P., Handwerker, A. L., and Bièvre, G. (2020). Life and death of slow-moving landslides. *Nature Reviews Earth and Environment*, 1(8), 404–419.
- Lanari, R., Casu, F., Manzo, M., Zeni, G., Berardino, P., Manunta, M., and Pepe, A. (2007). An overview of the small baseline subset algorithm: A DInSAR technique for surface deformation analysis. *Deformation and Gravity Change: Indicators of Isostasy, Tectonics, Volcanism, and Climate Change*, 637–661.
- Lanari, R., Mora, O., Manunta, M., Mallorquí, J. J., Berardino, P., and Sansosti, E. (2004). A small-baseline approach for investigating deformations on full-resolution differential SAR interferograms. *IEEE Transactions on Geoscience and Remote Sensing*, 42(7), 1377–1386.
- Langley, R. B., Teunissen, P. J. G., and Montenbruck, O. (2017). Introduction to GNSS. In *Springer handbook of global navigation satellite systems* (pp. 3–23). Springer.
- Lauer, I. (2021). *Kinematic GPS/GNSS Methods Manual*. <https://www.unavco.org/instrumentation/networks/status/all>
- Lazar, J., Shafri, H., and Savvaidis, P. D. (2003). *Existing Landslide Monitoring Systems and Techniques Related papers The Use of GPS in Mitigating and Managing Landslides Existing Landslide Monitoring Systems and Techniques*.

- Lee, S., Hong, S.-M., and Jung, H.-S. (2017). A support vector machine for landslide susceptibility mapping in Gangwon Province, Korea. *Sustainability*, 9(1), 48.
- Li, Y., Jiang, W., Zhang, J., Li, B., Yan, R., and Wang, X. (2021). Sentinel-1 SAR-Based coseismic deformation monitoring service for rapid geodetic imaging of global earthquakes. *Natural Hazards Research*, 1(1), 11–19.
- Liu, J., Wu, Z., and Zhang, H. (2021). Analysis of Changes in Landslide Susceptibility according to Land Use over 38 Years in Lixian County, China. *Sustainability*, 13(19), 10858.
- Loucks, E. D. (2018). *Documentation of Slope Failure Along Shoal Creek at Pease Park*. http://www.austintexas.gov/sites/default/files/files/Watershed/erosion/Pease_Park_Slope_Failure_Assessment_20180511_reduced.pdf
- Lu, Z., Kwoun, O., and Rykhus, R. (2007). Interferometric synthetic aperture radar (InSAR): its past, present and future. *Photogrammetric Engineering and Remote Sensing*, 73(3), 217.
- Maclay, R. W., and Small, T. A. (1983). Hydrostratigraphic subdivisions and fault barriers of the Edwards aquifer, south-central Texas, U.S.A. *Journal of Hydrology*, 61(1), 127–146. [https://doi.org/https://doi.org/10.1016/0022-1694\(83\)90239-1](https://doi.org/https://doi.org/10.1016/0022-1694(83)90239-1)
- Malczewski, J. (2000). On the use of weighted linear combination method in GIS: common and best practice approaches. *Transactions in GIS*, 4(1), 5–22.
- Mantovani, M., Bossi, G., Marcato, G., Schenato, L., Tedesco, G., Titti, G., and Pasuto, A. (2019). New Perspectives in Landslide Displacement Detection Using Sentinel-1 Datasets. *Remote Sensing 2019, Vol. 11, Page 2135*, 11(18), 2135. <https://doi.org/10.3390/RS11182135>
- Manzo, G., Tofani, V., Segoni, S., Battistini, A., and Catani, F. (2013). GIS techniques for regional-scale landslide susceptibility assessment: the Sicily (Italy) case study. *International Journal of Geographical Information Science*, 27(7), 1433–1452.
- Mao, Z., Yang, M., Bourrier, F., and Fourcaud, T. (2014). Evaluation of root reinforcement models using numerical modelling approaches. *Plant and Soil*, 381(1–2), 249–270. <https://doi.org/10.1007/S11104-014-2116-7>
- Martins, B. H., Suzuki, M., Yastika, P. E., and Shimizu, N. (2020). Ground surface deformation detection in complex landslide area—bobonaro, Timor-Leste—using SBAS DinSAR, UAV photogrammetry, and field observations. *Geosciences*, 10(6), 245.
- Mays, L. W. (1991). Flood Simulation for a Large Reservoir System in the Lower Colorado River Basin, Texas. *National Water Summary 1988-89: Hydrologic Events and Floods and Droughts*, 2375, 143.
- Moharrami, M., Naboureh, A., Gudiyangada Nachappa, T., Ghorbanzadeh, O., Guan, X., and Blaschke, T. (2020). National-scale landslide susceptibility mapping in Austria using fuzzy best-worst multi-criteria decision-making. *ISPRS International Journal of Geo-Information*, 9(6), 393.
- Moreira, A., Prats-Iraola, P., Younis, M., Krieger, G., Hajnsek, I., and Papathanassiou, K. P. (2013). A tutorial on synthetic aperture radar. *IEEE Geoscience and Remote Sensing Magazine*, 1(1), 6–43.
- Moresi, F. V., Maesano, M., Collalti, A., Sidle, R. C., Matteucci, G., and Scarascia Mugnozza, G. (2020). Mapping landslide prediction through a GIS-based model: A case study in a

- catchment in southern Italy. *Geosciences*, 10(8), 309.
- National Aeronautics and Space Administration (NASA). (2020). Interferometry - Get to Know SAR. Retrieved July 1, 2022, from <https://nisar.jpl.nasa.gov/mission/get-to-know-sar/interferometry/>
- Okeke, F. I. (2006). InSAR operational and processing steps for DEM generation. *Promoting Land Administration and Good Governance*, 1–13.
- Oliver, C., and Quegan, S. (2004). *Understanding synthetic aperture radar images*. SciTech Publishing.
- Pachauri, A. K., and Pant, M. (1992). Landslide hazard mapping based on geological attributes. *Engineering Geology*, 32(1–2), 81–100.
- Patil, V., Bizcarguenaga, M., Lieberknecht, K., and Felkner, J. (2021). Retrofitting solutions for a campus building to mitigate urban heat island in a hot humid climate. *Journal of Physics: Conference Series*, 2042(1), 012062. <https://doi.org/10.1088/1742-6596/2042/1/012062>
- Pepe, A., and Calò, F. (2017). A review of interferometric synthetic aperture RADAR (InSAR) multi-track approaches for the retrieval of Earth's surface displacements. *Applied Sciences*, 7(12), 1264.
- Plummer, H. J. (1949). *Foraminifera in Some Cretaceous Outcrops in Travis County, Texas*.
- Pour, A. B., and Hashim, M. (2017). Application of Landsat-8 and ALOS-2 data for structural and landslide hazard mapping in Kelantan, Malaysia. *Natural Hazards and Earth System Sciences*, 17(7), 1285–1303.
- Pourpeikari Heris, M., Bagstad, K. J., Troy, A. R., and O'Neil-Dunne, J. P. M. (2022). Assessing the Accuracy and Potential for Improvement of the National Land Cover Database's Tree Canopy Cover Dataset in Urban Areas of the Conterminous United States. *Remote Sensing*, 14(5), 1219.
- Prati, C., Ferretti, A., and Perissin, D. (2010). Recent advances on surface ground deformation measurement by means of repeated space-borne SAR observations. *Journal of Geodynamics*, 49(3–4), 161–170.
- Prudent, N., Houghton, A., and Lubert, G. (2016). Assessing climate change and health vulnerability at the local level: Travis County, Texas. *Disasters*, 40(4), 740–752. <https://doi.org/10.1111/DISA.12177>
- Psomiadis, E., Papazachariou, A., Soulis, K. X., Alexiou, D.-S., and Charalampopoulos, I. (2020). Landslide mapping and susceptibility assessment using geospatial analysis and earth observation data. *Land*, 9(5), 133.
- Raghuvanshi, T. K., Ibrahim, J., and Ayalew, D. (2014). Slope stability susceptibility evaluation parameter (SSEP) rating scheme—an approach for landslide hazard zonation. *Journal of African Earth Sciences*, 99, 595–612.
- Raghuvanshi, T. K., Negassa, L., and Kala, P. M. (2015). GIS based Grid overlay method versus modeling approach—A comparative study for landslide hazard zonation (LHZ) in Meta Robi District of West Showa Zone in Ethiopia. *The Egyptian Journal of Remote Sensing and Space Science*, 18(2), 235–250.
- Rahim, I., Ali, S. M., and Aslam, M. (2018). GIS Based landslide susceptibility mapping with application of analytical hierarchy process in District Ghizer, Gilgit Baltistan Pakistan.

Journal of Geoscience and Environment Protection, 6(2), 34–49.

- Rawat, M. S., Joshi, V., Rawat, B. S., and Kumar, K. (2011). Landslide movement monitoring using GPS technology: A case study of Bakthang landslide, Gangtok, East Sikkim, India. *Journal of Development and Agricultural Economics*, 3(5), 194–200.
- Reichenbach, P., Busca, C., Mondini, A. C., and Rossi, M. (2014). The Influence of Land Use Change on Landslide Susceptibility Zonation: The Briga Catchment Test Site (Messina, Italy). *Environmental Management*, 54(6), 1372–1384. <https://doi.org/10.1007/S00267-014-0357-0/TABLES/3>
- Reichenbach, Paola, Rossi, M., Malamud, B. D., Mihir, M., and Guzzetti, F. (2018). A review of statistically-based landslide susceptibility models. *Earth-Science Reviews*, 180, 60–91.
- Reigber, A., and Moreira, J. (1997). Phase unwrapping by fusion of local and global methods. *IGARSS'97. 1997 IEEE International Geoscience and Remote Sensing Symposium Proceedings. Remote Sensing-A Scientific Vision for Sustainable Development*, 2, 869–871.
- Roodposhti, M. S., Aryal, J., and Pradhan, B. (2019). A novel rule-based approach in mapping landslide susceptibility. *Sensors*, 19(10), 2274.
- Sadeh, Y., Cohen, H., Maman, S., and Blumberg, D. G. (2018). Evaluation of Manning's roughness coefficient in arid environments by using SAR backscatter. *Remote Sensing*, 10(10), 1505.
- Sarkar, S., Kanungo, D. P., and Mehrotra, G. S. (1995). Landslide hazard zonation: a case study in Garhwal Himalaya, India. *Mountain Research and Development*, 301–309.
- Scaioni, M., Longoni, L., Melillo, V., and Papini, M. (2014). Remote Sensing for Landslide Investigations: An Overview of Recent Achievements and Perspectives. *Remote Sensing*, 6(10), 9600–9652. <https://doi.org/10.3390/rs6109600>
- Shano, L., Raghuvanshi, T. K., and Meten, M. (2020). Landslide susceptibility evaluation and hazard zonation techniques—a review. *Geoenvironmental Disasters*, 7, 1–19.
- Shoal Creek Conservancy. (2020). Shoal Creek Landslide Update. Retrieved July 13, 2022, from <https://shoalcreekconservancy.org/shoal-creek-landslide-update/>
- Sidle, R. C., Pearce, A. J., and O'Loughlin, C. L. (1985). *Hillslope stability and land use*. American geophysical union.
- Sifa, S. F., Mahmud, T., Tarin, M. A., and Haque, D. M. E. (2020). Event-based landslide susceptibility mapping using weights of evidence (WoE) and modified frequency ratio (MFR) model: A case study of Rangamati district in Bangladesh. *Geology, Ecology, and Landscapes*, 4(3), 222–235.
- Sikora, F. J., and Moore, K. P. (2014). *Soil Test Methods From the Southeastern United States Southern Extension and Research Activity Information Exchange Group-6 (SERA-IEG-6)*. www.clemson.edu/sera6
- Simmons, M. T., Gardiner, B., Windhager, S., and Tinsley, J. (2008). Green roofs are not created equal: the hydrologic and thermal performance of six different extensive green roofs and reflective and non-reflective roofs in a sub-tropical climate. *Urban Ecosystems*, 11(4), 339–348. <https://doi.org/10.1007/s11252-008-0069-4>
- Small, D., and Schubert, A. (2008). Guide to ASAR geocoding. *ESA-ESRIN Technical Note RSL-ASAR-GC-AD*, 1, 36.

- Solari, L., Del Soldato, M., Raspini, F., Barra, A., Bianchini, S., Confuorto, P., Casagli, N., and Crosetto, M. (2020). Review of Satellite Interferometry for Landslide Detection in Italy. *Remote Sensing*, 12(8). <https://doi.org/10.3390/rs12081351>
- Soto, J., Galve, J. P., Palenzuela, J. A., Azañón, J. M., Tamay, J., and Irigaray, C. (2017). A multi-method approach for the characterization of landslides in an intramontane basin in the Andes (Loja, Ecuador). *Landslides*, 14(6), 1929–1947.
- Stokes, A., Norris, J. E., Van Beek, L. P. H., Bogaard, T., Cammeraat, E., Mickovski, S. B., Jenner, A., Di Iorio, A., and Fourcaud, T. (2008). How vegetation reinforces soil on slopes. *Slope Stability and Erosion Control: Ecotechnological Solutions*, 65–118. https://doi.org/10.1007/978-1-4020-6676-4_4
- Tagnon, B. O., Assoma, V. T., Mangoua, J. M. O., Douagui, A. G., Kouamé, F. K., and Savané, I. (2020). Contribution of SAR/RADARSAT-1 and ASAR/ENVISAT images to geological structural mapping and assessment of lineaments density in Divo-Oume area (Côte d’Ivoire). *The Egyptian Journal of Remote Sensing and Space Science*, 23(2), 231–241.
- Terzaghi, K., Peck, R. B., and Mesri, G. (1996). *Soil mechanics in engineering practice*. John Wiley and Sons.
- Tong, X., and Schmidt, D. (2016). Active movement of the Cascade landslide complex in Washington from a coherence-based InSAR time series method. *Remote Sensing of Environment*, 186, 405–415.
- United States Census Bureau. (2021). American Fact Finder: Population and Housing Unit Estimates. In <https://www.census.gov/programs-surveys/popest/data/data-sets.html>. <https://www.census.gov/programs-surveys/popest/data/data-sets.html>
- Vallone, P., Giammarinaro, M. S., Crosetto, M., Agudo, M., and Biescas, E. (2008). Ground motion phenomena in Caltanissetta (Italy) investigated by InSAR and geological data integration. *Engineering Geology*, 98(3–4), 144–155.
- Varnes, D. J. (1958). Landslide types and processes. *Landslides and Engineering Practice*, 24, 20–47.
- Varnes, D. J. (1978). Slope movement types and processes. *Special Report*, 176, 11–33.
- Wachal, D. J., and Hudak, P. F. (2000). Mapping landslide susceptibility in Travis County, Texas, USA. *GeoJournal*, 51(3), 245–253. <https://doi.org/10.1023/A:1017524604463>
- Wade, S., Ndoye, A., and Mbaye, M. (2001). *Téléphone : (221) 825 25 30*. 2(2), 18.
- Walker, J. P., Houser, P. R., and Willgoose, G. R. (2004). Active microwave remote sensing for soil moisture measurement: a field evaluation using ERS-2. *Hydrological Processes*, 18(11), 1975–1997.
- Wang, L., Qiu, H., Zhou, W., Zhu, Y., Liu, Z., Ma, S., Yang, D., and Tang, B. (2022). The Post-Failure Spatiotemporal Deformation of Certain Translational Landslides May Follow the Pre-Failure Pattern. *Remote Sensing*, 14(10), 2333.
- Weeks, A. W. (1945). Balcones, Luling, and Mexia Fault Zones in Texas1. *AAPG Bulletin*, 29(12), 1733–1737. <https://doi.org/10.1306/3D9337B0-16B1-11D7-8645000102C1865D>
- Werner, C., Wegmüller, U., Strozzi, T., and Wiesmann, A. (2002). Processing strategies for phase unwrapping for INSAR applications. *Proceedings of the European Conference on Synthetic Aperture Radar EUSAR*.

- Wieczorek, G. F., and Snyder, J. B. (2009). Monitoring slope movements. *Geol. Monit*, 1, 245–271.
- Wu, T. H. (1984). Effect of vegetation on slope stability. *Transportation Research Record*, 965, 37–46.
- Yalcin, A. (2007). The effects of clay on landslides: A case study. *Applied Clay Science*, 38(1–2), 77–85.
- Yalcin, A. (2008). GIS-based landslide susceptibility mapping using analytical hierarchy process and bivariate statistics in Ardesen (Turkey): comparisons of results and confirmations. *Catena*, 72(1), 1–12.
- Yilmaz, C., Topal, T., and Süzen, M. L. (2012). GIS-based landslide susceptibility mapping using bivariate statistical analysis in Devrek (Zonguldak-Turkey). *Environmental Earth Sciences*, 65(7), 2161–2178. <https://doi.org/10.1007/s12665-011-1196-4>
- Young, K. (1977). Guidebook to the geology of Travis County. In *Walter Geology Library*. The Student Geology Society, The University of Texas.
- Young, R., and Norby, L. (2009). *Geological monitoring*. Geological Society of America.
- Zebker, H. A., Villasenor, J., and others. (1992). Decorrelation in interferometric radar echoes. *IEEE Transactions on Geoscience and Remote Sensing*, 30(5), 950–959.
- Zhao, C., and Lu, Z. (2018). Remote sensing of landslides-A review. In *Remote Sensing* (Vol. 10, Issue 2). <https://doi.org/10.3390/rs10020279>
- Zhou, X., Chang, N.-B., and Li, S. (2009). Applications of SAR interferometry in earth and environmental science research. *Sensors*, 9(3), 1876–1912.

VITA

Rosbeidy Hernandez was born on May 25, 1989, in Maracay, Venezuela. She is the third child of Roberto Hernandez and Carmen Marin. In 2014, she received a bachelor's degree in Geological Engineering from the Universidad Central de Venezuela in Caracas. During her undergrad experience, she was a student assistant covering a wide variety of responsibilities in the Geology and Petrology Lab 330. In addition, she was a member of the Student Geoscience Foundation.

After receiving her bachelor's degree in 2015, she worked simultaneously in two part-time jobs. The first one was at the Venezuelan Seismological Research Institute (FUNVISIS), where she contributed to a regional geological mapping project in northern Venezuela and participated in several natural hazard assessments around the country. The second job was leading laboratory analyses and generating technical reports for a road tunneling project contract with CienFuegos Consultores y Gerencia de Proyectos.

In 2016, she decided to move abroad to learn a second language at the Texas Christian University (TCU) intensive English program in Fort Worth, Texas. After a short period in the English program, she decided to transfer to the Tarrant Community College to obtain an Associate Degree in Applied Science in Geographical Information Systems (GIS). After graduation, she joined the Trinity Metro- Tarrant County Public Transportation as a GIS Data Coordinator from 2019 to 2020. After working for a year in the GIS field, she decided to go back to her professional roots and combine her GIS skills with geological studies to pursue a master's degree at TCU.

After graduation, she wishes to find a job that combines her geologic knowledge and GIS skills in a company that allows her to work with natural hazard mitigation

ABSTRACT

MAPPING LANDSLIDE SUSCEPTIBILITY AND GROUND DISPLACEMENT ASSESSMENT OF AUSTIN CITY AND ITS SURROUNDINGS

By Rosbeidy Hernandez, MSc., 2022
Department of Geological Science
Texas Christian University

Thesis Advisor: Dr. Esayas Gebremichael, Assistant Professor of Geology

Recently, the city of Austin and its suburbs have witnessed high population growth that has driven communities to reside in areas susceptible to landslide hazards. This study integrated multiple datasets using different techniques to assess the landslide hazards susceptibility in the area, as well as slow-moving slide identification areas and their displacement rate quantification. The results are: (a) a landslide susceptibility map (LSM) derived by combining six factors and variables that could influence the incidence of landslides indicates that 16.8% of the study area is highly susceptible to the hazard. These areas lie on moderate to steep slopes ($> 14^\circ$) proximal to geological structures and drainage networks, have low to moderate vegetation cover, and receive moderate amounts of annual rainfall (> 870 mm). The main geologic units include the fractured and weathered limestones from the Eagle Ford, Georgetown, Buda Formations, the Del Rio Formation, and patches of gravel and terrace deposits; (b) Small Baseline Subset (SBAS) interferometric analysis technique was applied on fifty-three Sentinel-1 images, the results calibrated and validated using permanent and campaign Global Navigation Satellite System (GNSS) datasets, to detect slow-moving type landslides and quantify their rates. The results indicate that the slow-moving slides across the study area move at displacement rates ranging from -1 to -3.06 mm/yr. The analysis shows a high spatial correlation between the medium-high and high landslide susceptible areas delineated using the LSM and SBAS method in the north and northwestern parts of the study area; (c) the findings of the present study indicate that the interactions of water percolating through the fractured Buda Formation with the montmorillonite-

and kaolinite-bearing Del Rio Formation resulted in a buildup of shear stress and initiated the displacement of the slope material. Intense rainfall episodes hastened the displacement rates and eventually led to the slope failures. The slope failure mechanism put forward in this study was assessed through a close investigation of the Pease Park (Shoal Creek) landslide through lithologic sample analysis and a 3D model derived using data acquired using Unmanned Aerial Vehicle (UAV).